

# Adaptive electronics for photovoltaic, photoluminescent and photometric methods in power harvesting for wireless wearable sensors

Received: 13 November 2024

Accepted: 9 June 2025

Published online: 01 July 2025

 Check for updates

Chanho Park<sup>1,2,22</sup>, Do Yun Park<sup>3,22</sup>, Haohui Zhang <sup>4,22</sup>, Da Som Yang<sup>5,22</sup>, Catherine R. Redden<sup>6</sup>, Seonggwang Yoo <sup>1,2,7</sup>, Tae Wan Park <sup>1,2</sup>, Mingyu Zhou <sup>1,2,8</sup>, Jae-Young Yoo <sup>9</sup>, Youngmin Sim<sup>10</sup>, Abraham Vázquez-Guardado <sup>11,12</sup>, Seung Yun Heo<sup>1,2</sup>, Raudel Avila<sup>13</sup>, Zhao-Bang Hou <sup>14</sup>, Jiwon Kim <sup>15</sup>, Hak-Young Ahn <sup>1,2</sup>, Youngdo Kim<sup>1,2</sup>, Seyong Oh <sup>16</sup>, Jae-Hwan Kim<sup>1,2</sup>, Jason Baek<sup>17</sup>, Anthony Banks<sup>1,2</sup>, Aimen F. Shaaban <sup>6,18</sup>, Yonggang Huang <sup>1,4,19,20</sup> , Kyeongha Kwon <sup>3,10</sup>  & John A. Rogers <sup>1,2,8,19,21</sup> 

The increasing demand for continuous, comprehensive physiological information captured by skin-interfaced wireless sensors is hindered by their relatively high-power consumption and the associated patient discomfort that can follow from the use of high capacity batteries. This paper presents an adaptive electronics platform and a tri-modal energy harvesting approach to reduce the need for battery power. Specifically, the schemes focus on sensors that involve light in their operation, through use of (i) photometric methods, where ambient light contributes directly to the measurement process, (ii) multi-junction photovoltaic cells, where ambient light powers operation and/or charges an integrated battery, and (iii) photoluminescent packaging, where ambient light activates light-emitting species to enhance the first two schemes. Additional features of interest are in (i) in-sensor computational approaches that decrease the bandwidth and thus the energy consumption in wireless data communication and (ii) radio frequency power transfer for battery charging. These ideas have utility across broad other classes of wearable devices as well as small, portable electronic gadgetry.

The emergence of medical-grade wearable sensors promises to radically alter approaches to health care, with significant potential for reduced costs and improved patient outcomes<sup>1–5</sup>. For skin-interfaced devices of these types, reductions in the mechanical stiffness, size and weight can improve patient adherence by minimizing discomfort, ultimately to imperceptible levels<sup>6–9</sup>. In many cases, the batteries dominate these properties<sup>10–12</sup>. As a result, significant interest is in ultralow power

electronics, self-powered sensors and components for harvesting energy from the body or the environment<sup>13–16</sup>. Diverse options exist, ranging from those based on mechanical and thermal processes to schemes that exploit ambient light and even humidity in the air<sup>17–22</sup>. Recent review articles summarize these and other mechanisms<sup>23–26</sup>.

This work introduces adaptive electronic schemes and three complementary methods in light-based power harvesting for skin-

A full list of affiliations appears at the end of the paper.  e-mail: [y-huang@northwestern.edu](mailto:y-huang@northwestern.edu); [kyeongha@kaist.ac.kr](mailto:kyeongha@kaist.ac.kr); [jrogers@northwestern.edu](mailto:jrogers@northwestern.edu)

interfaced, wireless sensors that rely on optical principles. Our interest in these specific classes of devices is that the light sources required for these devices often dominate the total power consumption, and thus represent the main consideration in battery capacity needed to meet requirements for operating lifetime. The first method, referred to as photometric, uses ambient light as the basis for part or all of the sensing process. The second relies on photovoltaics in a circuit design and dual-battery configuration that allows direct support of device operation and/or for storage and subsequent utilization. The third exploits photoluminescence (PL) in the structural parts of the sensors to enhance the first two mechanisms in dim light and to enable their use even in the dark. Besides adaptive balancing of these three sources of power, the electronics also perform real-time in-sensor computing to minimize power necessary for wireless data transfer. Various classes of skin-interfaced devices illustrate these concepts in practical applications and use scenarios. Besides health monitoring, the results presented here may have additional utility in a range of portable consumer gadgetry.

## Results

### Multimodal light harvesting mechanisms

A sensor for dual-wavelength photoplethysmography (PPG) provides an illustrative example of all of these concepts in a single integrated system, as shown in Fig. 1a, b. The first design feature allows ambient light to pass through a window that transmits red and infrared (IR) wavelengths, to illuminate regions of the skin adjacent to a pair of photodetectors (PDs) with responses aligned to these same two wavelengths, as in Fig. 1a<sup>27,28</sup>. Adaptive control electronics activate two separate light emitting diodes (LEDs), also at these wavelengths, to complement the optical power provided by the ambient light, as necessary depending on the ambient illumination conditions. Specifically, the adaptive electronics drive these LEDs at currents just sufficient to maintain an adequate signal-to-noise ratio in the measurements, in a manner that accounts for the contribution of ambient light.

The second feature is a high efficiency photovoltaic (PV) cell and corresponding circuit for exploiting power generated in this fashion, also in an adaptive mode that depends on power requirements and ambient light intensity (Fig. 1b and Supplementary Fig. 1). Here, the PV cell charges one of two batteries, referred to as the PV battery. The base battery can be charged wirelessly through inductive coupling mechanisms<sup>6</sup>. Depending on the power generation from the PV cell and the power consumption of the sensor, the system adaptively changes the power source. Details appear in Fig. 2 and Supplementary Note 1.

The third feature, which complements the first two, exploits PL associated with microparticles (~60  $\mu\text{m}$  in diameter, Supplementary Fig. 2) of strontium aluminate mixed into the surrounding silicone encapsulating structure<sup>29</sup>. Ambient light activates these microparticles such that subsequent PL emission can contribute to the photometric and photovoltaic processes, of value in cases of dim light or dark conditions. Diffusion theory of light propagation captures quantitative aspects of this process as well as the photometric mechanism, as described subsequently.

The electronics not only adaptively control these harvesting mechanisms, but they also further improve the performance of the system by reducing the amount of data that must be transmitted wirelessly in Fig. 1a. Specifically, algorithms executed on the Bluetooth Low Energy (BLE) System-on-a-Chip (SoC) determine the heart rate (HR) and the blood oxygen saturation ( $\text{SpO}_2$ ) from the responses of the PDs. Only these parameters, and not the full raw data streams, then pass wirelessly to an external reader. For the parameters used here, this in-sensor computational scheme reduces the wireless data transmission requirements from 400 B/s to 4.00 B/s. Details appear in the following section. The images in Fig. 1c show the sensor in bright and dim ambient light and in the dark.

Similar harvesting mechanisms and power-efficient, adaptive electronics apply to other classes of wireless wearable sensors. In an example of a sensor configured to measure exposure dose associated with blue light, this light itself powers the sensing mechanism through photometrics while ambient light across the visible spectrum assists in the supply of power to the electronics through photovoltaics. Another example incorporates chemical assays and microfluidic structures to measure the rate of production and total loss of eccrine sweat, along with its pH and concentration of chloride and glucose, through colorimetric schemes enabled by all three light-harvesting mechanisms. Detailed descriptions appear subsequently. A final section describes the integration of all of these measurement modalities, harvesting schemes, and control electronics into a single platform.

### Adaptive power management system

The adaptive power management (aPM) system is central to the overall operation of the system. Power to operate the electronics originates from two sources (1) electromagnetic induction at a frequency of 13.56 MHz from an external transmission (TX) coil to a device-integrated receiver (RX) coil, and (2) output of the device-integrated PV cell. Based on the charge status of the batteries and the external energy harvesting conditions, as depicted in Fig. 2a, the system supports 11 distinct power configurations for the sensor, as detailed in Supplementary Note 1 and Supplementary Figs. 3–6. A representative four-block diagram of the aPM system appears in Fig. 2b.

When the PV battery voltage ( $V_{\text{PV}}$ ) exceeds 3.60 V, the system operates using power sourced from the PV cell, as shown in configurations (1) and (2). In configuration (1), where the power generated by the PV cells ( $P_{\text{cell}}$ ) surpasses power consumption of the sensor ( $P_{\text{sensor}}$ ), the cell supplies power to the sensor while simultaneously charging the PV battery up to 4.12 V, thereby providing over-discharge protection (Supplementary Fig. 7). As shown in Supplementary Fig. 5, if both  $V_{\text{PV}}$  and the voltage of PV cell ( $V_{\text{cell}}$ ) exceed 4.12 V, the PV cell disconnects from the photovoltaic energy harvesting integrated circuit (PEH-IC) to prevent overcharging, with the PV battery continuing to serve as the power source. In configuration (2), when the  $P_{\text{cell}}$  is insufficient to meet the demands of  $P_{\text{sensor}}$ , the PV battery supplements to reach the necessary power. In both configurations, the PEH-IC outputs a regulated 3.30 V, the power multiplexer (pMUX) disconnects the base battery, and the low dropout (LDO) regulator ensures a stable 3.00 V output. The results for use of excess power to charge the PV battery while the PV cell power operation of the device are shown in Supplementary Fig. 8.

If  $V_{\text{PV}}$  falls below 3.6 V due to battery discharge, the system transitions to configurations (3) and (4) by disconnecting the PEH-IC from the pMUX to prevent further discharge of the PV battery. In configuration (3), should the PV cell generate a voltage above 50 mV, the PEH-IC boosts this voltage up to 4.12 V and charges the PV battery up to 3.67 V. During this charging phase, the PV cell serves primarily to charge the PV battery, while the electromagnetic harvesting system can provide additional power. As mentioned previously, the RX coil receives power from the TX coil at a resonant frequency of 13.56 MHz (Supplementary Fig. 9). This AC voltage is rectified as DC voltage through a diode bridge rectifier, and a charge pump (CP) converter regulates this voltage as the output to 4.12 V. The CP converter, base battery, and pMUX connect in parallel, enabling the CP converter to charge the base battery while simultaneously powering the sensor. The PPG sensor temperature increases during battery charging from electromagnetic harvesting. Increasing the power to the TX coil leads to further increases in temperature. The maximum temperature occurs at the CP component, as shown in Supplementary Fig. 10. At a TX power of 2 W, 4 W, and 8 W, the temperature reaches 28.4 °C, 32.1 °C and 37.3 °C, all of which lie below the threshold for burn injury (44 °C). Furthermore, the encapsulation layer prevents direct thermal transfer from the device to the skin, enhancing thermal safety

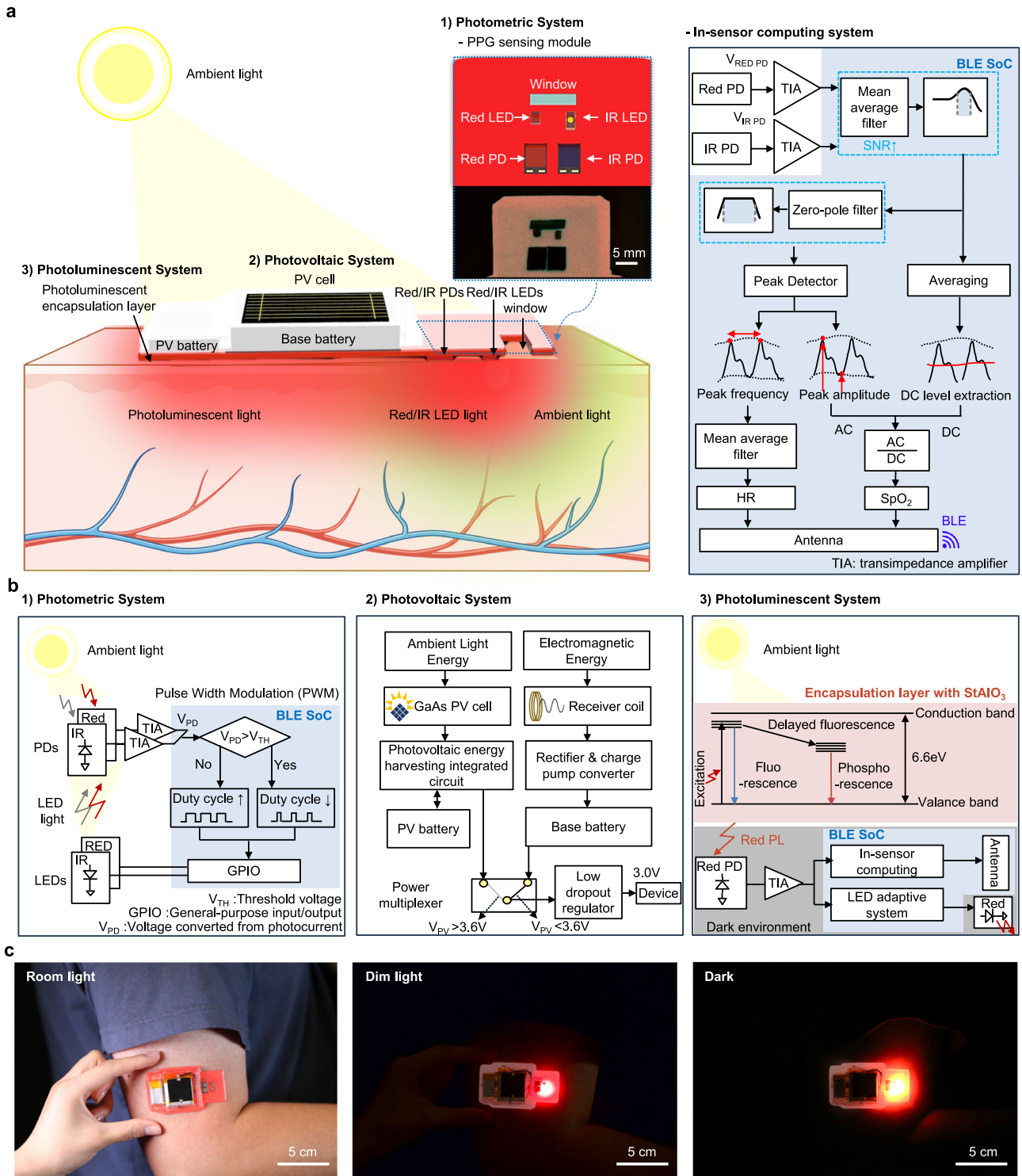


**Fig. 1 | Energy harvesting by photoluminescence, photovoltaics and photometrics in a sensor for monitoring heart rate (HR) and blood oxygen saturation (SpO<sub>2</sub>) through PPG sensing with in-sensor computation.** a Schematic illustration of the sensor and operational mechanisms with a block

diagram of in-sensor computation. Created in BioRender<sup>39</sup>. **b** Block diagrams of the strategies for low-power operation. **c** The images show a sensor adhered to the forearm under room light, dim light, and dark environments.

for long-term wear<sup>30</sup>. In this configuration, the pMUX disconnects the PEH-IC and connects to the base battery, with the LDO maintaining a stable 3.00 V output. Additionally, if there is no power from the TX coil, the pMUX transmits the voltage from the base battery, maintaining the same configuration as in (3), with the LDO generating a stable 3.00 V output. Throughout this process, the PV cell charges the

PV battery. If  $V_{PV}$  exceeds 3.67 V, the system reverts to configurations (1) or (2). As depicted in configuration (4), if the PV cell generates less than 50 mV, the system relies solely on the previously charged base battery or wireless transfer for power by disconnecting the PEH-IC from the pMUX and connecting the base battery to the pMUX while awaiting sufficient light for harvesting. Through these dynamic circuit

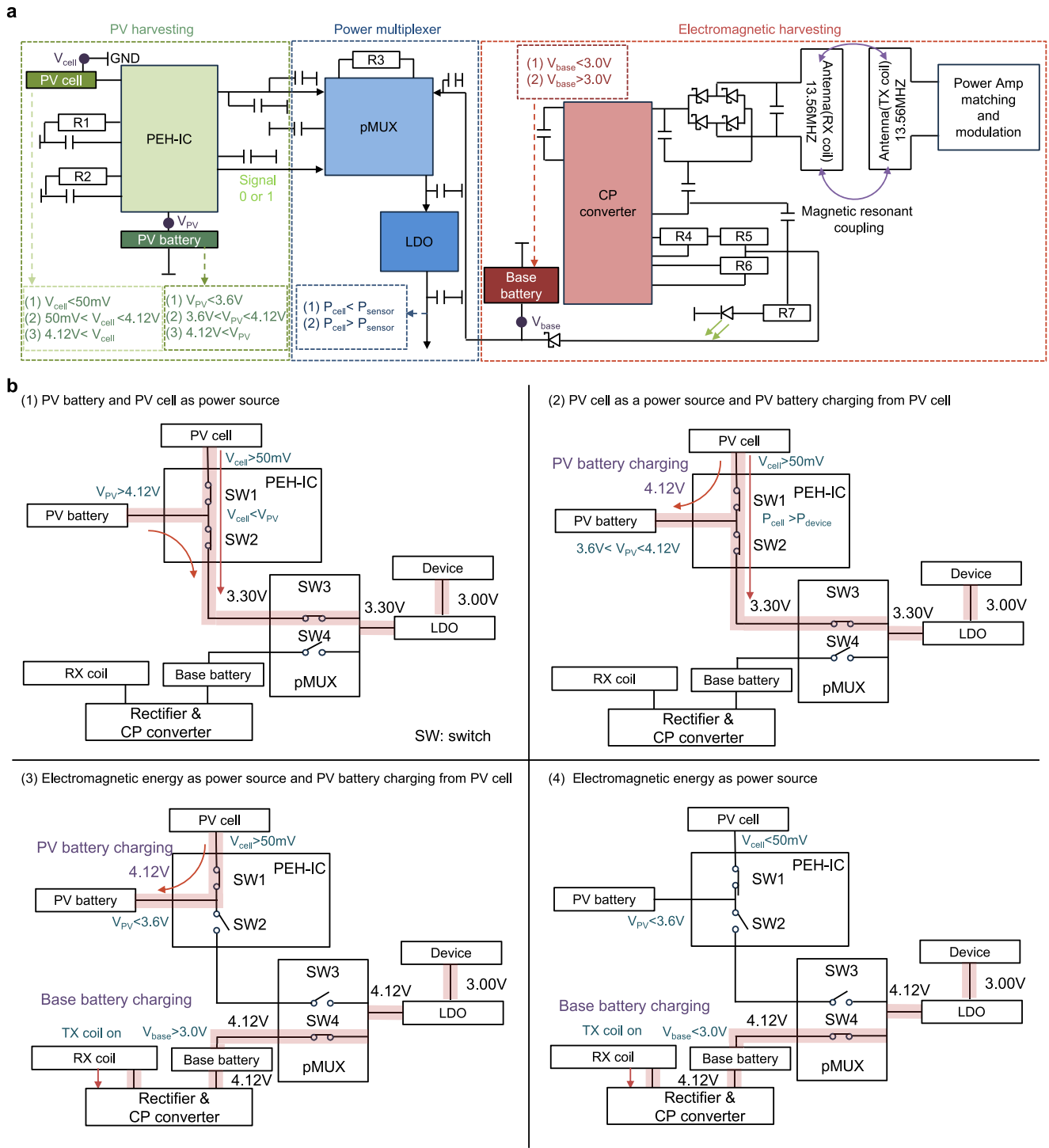


**Fig. 2 | Light adaptive power management system with a PV cell and electromagnetic harvesting.** **a** Schematic illustration of the circuit diagram of the adaptive power management (aPM) module, including PV harvesting unit, power switching module, and electromagnetic harvesting module, with associated

conditions for changing the power source. **b** Four representative block diagrams of the aPM module show different connections of the power sources: PV cell, PV battery, and electromagnetic harvesting by adaptation to ambient light conditions.

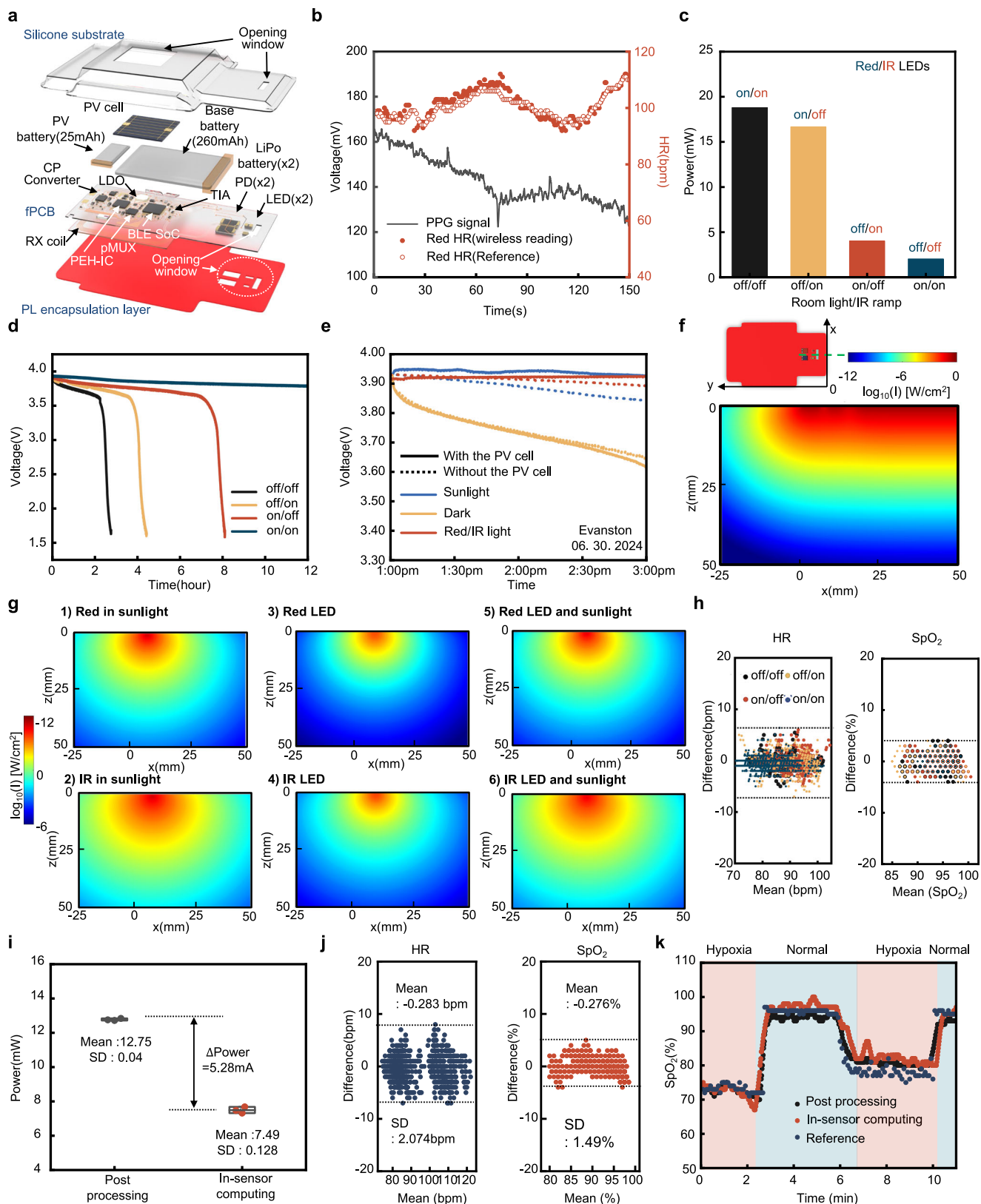
connection controls between the PV cells and batteries, the system ensures a stable voltage supply to the sensor, while automatically adapting to varying ambient light conditions.

**PPG Sensor**

The electronics for the wireless PPG sensor satisfy three main objectives in efficient, low-power operation: (1) dual (solar/electromagnetic) energy harvesting, (2) adaptive LED control, and (3) in-sensor

computing. The sensor, illustrated in Fig. 3a, consists of soft, silicone encapsulating structures, electronic components and a flexible printed circuit board (fPCB; for details, see Methods, and Supplementary Note 2, and Supplementary Figs. 11, 12).

The encapsulating structure includes widening windows that permit the transmission of LED and ambient light to the skin, along with transmission of the latter to the PV cell and the PL material incorporated into bottom layer (Supplementary Fig. 12). As mentioned



previously, the PL layer serves as an energy storage medium that absorbs and later emits light for PPG signal acquisition (Supplementary Fig. 13). With an appropriately designed transparent encapsulation structure, charging from ambient light is possible, as shown in Fig. 3b. By this mechanism, exposure to  $\sim 500$  W/m<sup>2</sup> of sunlight for 10 min allows for measurements of HR for up to 2.5 min

in the dark. Table S1 summarizes information on the human subject participants in these studies. During one of our indoor activities, the PL encapsulation layer decreased the power consumption from 3.69 mW to 3.42 mW of the PPG sensor compared to the non-PL embedded encapsulation layer (Supplementary Fig. 14). Furthermore, battery discharge studies for long-term energy consumption

**Fig. 3 | Light-adaptive, power-efficient sensor for HR and SpO<sub>2</sub> by PPG measurements.** **a** Exploded view schematic illustration that highlights the energy harvesting system, a light-adaptive PPG sensing module, a PV cell, a BLE communication module, a pair of LiPo batteries, all attached via an fPCB platform and housed in a silicone encapsulation structure. **b** The PPG signal (black) and calculated HR value (red filled circle) measured from the response of the red PD activated with light from the PL component of the encapsulation structure. Measurements involve a period of 2.5 minutes in dark conditions after exposing the PL component to light from the sun. The red unfilled circles in the graph correspond to HR values measured from a reference system (Dash-3000, GE) on the finger. **c** Power consumption for measurements of HR and SpO<sub>2</sub> for four different ambient light conditions by controlling room light and an IR lamp, at 3 V operation. **d** Dependence of  $V_{PV}$  on operation time for different ambient light conditions. **e** Dependence of  $V_{PV}$  on time for sensors with and without the aPM module in a dark or sunlight environment. **f** Results of diffusion theory simulation of light propagation in the near-surface region of the skin due to illumination from PL. **g** Results of diffusion theory for red and IR light from the LEDs, and from sunlight that passes

through windows in the top of the encapsulation structure. **h** Bland-Altman (BA) plots of HR and SpO<sub>2</sub> measured using the sensor and reference system under four different ambient light conditions from three healthy adult subjects, using a breath hold method to modulate SpO<sub>2</sub>. **i** The power consumption of the App with in-sensor computing (60 Hz sampling rate) or without in-sensor computing (60 Hz sampling rate) for measurements of HR and SpO<sub>2</sub> ( $n = 3$ , using different experimental units). The top and bottom lines represent the minimum and maximum values, and the box plot represents the interquartile range (IQR), which spans from the 25th to the 75th percentiles. Whiskers extend to 1.5 times the IQR. The circle shape within each box indicates the median of the dataset. **j** BA plots of HR and SpO<sub>2</sub> values determined using in-sensor computing and using the reference sensor for three healthy adult participants in air with controlled oxygen concentration ( $n = 3$ , using different experimental subjects). **k** Measurements of SpO<sub>2</sub> in a mouse model, determined using a commercial PPG sensor (blue) and using the sensor with post-processing (black) and in-sensor computing (red) under room lighting during cycles of normal (100% oxygen) and hypoxia states.

show an 8.6% operational time increase of the PPG sensor with the PL encapsulation layer.

During operation, the BLE SoC (Fig. 1a, b) employs two analog-to-digital converters (ADCs) to read the values of voltages from the red and IR PDs ( $V_{PD}$ ). Based on these data, the system performs (1) adaptive LED control and (2) in-sensor computing. This approach optimizes the overall power consumption, thereby extending the operational lifespan of the sensor and ensuring efficient PPG signal acquisition and essential data (SpO<sub>2</sub> and HR) extraction. The adaptive LED control system minimizes power consumption by leveraging ambient and PL light sources, while ensuring sufficient signal-to-noise ratio (SNR) in the data for accurate sensing. The system calculates the average light intensity from PD readings (100 Hz) over 10 s, as a basis for adjusting the brightness of the LED to maintain a constant total illumination from the combined effects of ambient, PL, and LED light. When  $V_{PD}$  deviates from a predefined threshold ( $V_{TH}$ ; 0.42 V), the system adjusts the pulse train from the general purpose input/output (GPIO) to each LED separately, either increasing or decreasing the duty cycle appropriately. The pulse-width modulation (PWM) continues until the PD readings align with the threshold, leading to longer 'on' or 'off' periods (higher and lower duty cycles, respectively) to increase or decrease the average LED brightness, respectively (Supplementary Fig. 15). This process ensures that the PD readings (total light intensity) remain constant, thereby facilitating accurate, consistent sensing (Supplementary Fig. 15 and Note 3)<sup>31</sup>. At low light intensity (0.62 mW), the PPG signal is continuously measured during light adaptation. At high light intensity (2.18 mW and 39.38 mW), fluctuations in the signal from the signal's amplification is generated in under 2 seconds. However, short fluctuations are compensated by a digital filter during in-sensor computing for continuous SpO<sub>2</sub> measurements. The minimum response time of adaptive LED control is 10 ms, sufficiently short to avoid any temporal lag. In addition, the light control is based on photovoltage with a minimum resolution of 0.146 mV, and the sensitivity of light control is followed by the sensitivity of photovoltage about each light source. Supplementary Fig. 16 shows the sensitivity at each light source from the relation between photovoltage and absolute light intensity as 0.0245 V/mW (red PD for red LED), 0.1326 V/mW (IR PD for IR LED), 0.1559 V/mW (red PD for sunlight), 0.0208 V/mW (IR PD for sunlight), 0.01769 V/mW (red PD for room light), and 0.0006 V/mW (red PD for PL light). Furthermore, because of the weak absolute intensities of PL light compared to other light sources (LED light: 1.228 mW, room light: 10.035 mW, sunlight: 29.501 mW, PL light: 0.616  $\mu$ W), during the light adaptive process, the PL light source does not lead to artifacts (Supplementary Fig. 17).

Figure 3c shows values for the power consumption across four scenarios based on illumination from a standard room light (E355998

LED Lamp, Great Eagle) and an IR lamp (CM-IRP6-850, CMVision): both off (black; darkness), only the IR lamp (yellow; intensity: 266.35 W/m<sup>2</sup>), only room light (red; intensity: 283.15 W/m<sup>2</sup>), and both the room light and the IR lamp (blue; intensity: 283.15 W/m<sup>2</sup> and 266.35 W/m<sup>2</sup>, respectively), with corresponding red/IR LED states (on/on, on/off, off/on, and off/off, respectively) (Supplementary Fig. 18). The latter case, equivalent to typical sunlight conditions (both LEDs off), yields an 86.22% reduction in power consumption compared to conditions of darkness (both LEDs on). The emission spectra of room lights, IR lamps and the red/IR LEDs are in Supplementary Fig. 19. The red LED has an emission range of 570–650 nm with a peak at 621 nm, while the IR LED has an emission range of 760–980 nm with a peak at 903 nm. The voltage profiles of the PV battery during different modes of operation quantify the utility of the adaptive LED control (Fig. 3d) and harvesting (Fig. 3e) processes. Figure 3d illustrates the discharge behaviors during PPG measurements for the aforementioned four illumination scenarios with adaptive LED control but without the PV cell. Figure 3e demonstrates the extended operating time afforded by the energy harvesting capabilities of the PV cell (Supplementary Note 4). Depending on the ambient light intensities, the power source changes between PV battery and base battery. During the transition of power sources, the aPM module provides two different voltages: 3.0 V (power source: PV battery) and a voltage for the base battery (power source: base battery). However, LDO tuned these voltages to stable 3.0 V and influenced no discontinuous fluctuations in the PPG signals from the power source transitions in Supplementary Fig. 20.

The diffusion theory of light propagation determines the distribution of light intensity ( $I$ ) across the cross section of the underlying skin, as delineated by green lines in the inset of Fig. 3f, with both LEDs off and PL light on in darkness (Fig. 3f). Figure 3g illustrates the distribution under varied light conditions, maintaining a constant total light intensity of 578.28 W/m<sup>2</sup> across multiple source combinations: (1) red and (2) IR illumination (578.28 W/m<sup>2</sup>) from sunlight, (3) red LED or (4) IR LED, and (5) equal contributions (289.14 W/m<sup>2</sup> each) from red LED and sunlight or (6) IR LED and sunlight. Supplementary Fig. 21 shows the distribution for various combinations of sunlight and LED illumination that sum to 1 W (Supplementary Note 5).

Basic tests involve measurements of HR and SpO<sub>2</sub> from the index finger of three healthy male subjects (age range: 33–34, Table S1) under the four illumination scenarios described in Fig. 3c, using a clinical reference device (Dash-3000, GE healthcare) and the sensor after calibration (see Supplementary Note 6 and Supplementary Fig. 22)<sup>32</sup>. The calibration operates whenever the light adaptation starts, with the formula  $SpO_2 = q_1 \cdot R \times q_2$ .  $q_2$  is computed from diffusion theory, and  $q_1$  is calculated by comparing the R-value for the same SpO<sub>2</sub> value before the light adaptive process and after the light adaptive process. Therefore, as shown in Supplementary Fig. 22g, under consecutive

light changes, SpO<sub>2</sub> is measured consistently. Bland-Altman (BA) plots (difference plots) in Fig. 3h show overlaid data from the three subjects while breath holding or at rest under four scenarios. Individual scenario data are in Supplementary Fig. 23. The HR and SpO<sub>2</sub> values for each subject as a function of time are in Supplementary Figs. 23, 24. The results (sample size:  $n \geq 590$  for each scenario) indicate good agreement between the sensor and reference values. With both LEDs inactive, under sufficient ambient light (both room light and IR lamp on; intensity: 160 W/m<sup>2</sup> and 270 W/m<sup>2</sup>, respectively), the HR and SpO<sub>2</sub> measurement errors (mean  $\pm$  standard deviation) are  $0.56 \pm 1.10$  bpm and  $0.02 \pm 1.60\%$ , respectively, which are comparable to the errors ( $0.29 \pm 1.10$  bpm and  $0.01 \pm 1.10\%$ ) with both LEDs active (in darkness). This finding validates the utility of ambient light as an alternative to LEDs. The impact of skin tone on the measurement accuracy of HR and SpO<sub>2</sub> is shown in Supplementary Fig. 25. Several studies have highlighted that the accuracy of PPG sensor can be influenced by skin pigmentation, primarily due to variations in photon scattering associated with melanin concentration in the skin<sup>33,34</sup>. While a light-adaptive system compensates for signal loss due to skin pigmentation, changes in the calibration factor may negatively impact measurement consistency. As shown in Supplementary Fig. 25, such changes lead to increased mean errors and standard deviations in both HR and SpO<sub>2</sub> measurements for individuals with lighter (including Fitzpatrick skin type II) and darker skin tones (Fitzpatrick skin types V) as in Fig. 3h. Supplementary Fig. 26 illustrates temperature variations at the LED top surface of the sensor, with a maximum difference of 0.35 °C between scenarios with both LEDs inactive and active. Supplementary Figs. 27 and 28 shows the results for SpO<sub>2</sub> and HR from the index finger of a healthy male subject (age: 32) in sunlight only (intensity: 663.60 W/m<sup>2</sup>) and from various body sites (earlobe, neck, big toe) with room lights only (intensity: 163.28 W/m<sup>2</sup>), respectively.

Standard PPG sensors generate data at a high rate (e.g. 6000 readings per minute at a 100-Hz sampling rate), whereas back-end data acquisition and processing units typically output single values of SpO<sub>2</sub> and HR every minute or second. Wireless transmission of significant amounts of data can limit the system performance in terms of energy efficiency, speed, and data security. As an additional advance to complement the light utilization strategies introduced here, the sensors exploit the BLE SoC for in-sensor computing to reduce the amount of wireless data transfer. The computational steps include digital filtering, peak detection, and averaging of raw data (100 Hz) to yield a single value for SpO<sub>2</sub> and HR every second (Supplementary Fig. 29 and Supplementary Note 7). The sensor without in-sensor computing, which offloads post-processing to a smartphone application (App), and a personal computer (PC) does not consume power for computing but must transmit significant amounts of data. The consequence is that the total current consumption (446.00  $\mu$ W) is comparable to that of the in-sensor computing sensor (485.00  $\mu$ W). Supplementary Fig. 30 shows results for data sampling rates of 1 Hz (481.05  $\mu$ W) and 60 Hz (485.18  $\mu$ W) for in-sensor computing sensors. Analysis of the power consumption of the App (dumpsys; Android Studio, Google) shows, however, that in-sensor computing reduces the current consumption of the App by 5.28 mA compared to the case without in-sensor computing, for HR and SpO<sub>2</sub> as shown in Fig. 3i for the case of three measurement intervals of 5 min at a sampling rate of 1 Hz. The BA plot (difference) in Fig. 3j highlights agreement between values of HR and SpO<sub>2</sub> determined under illumination from both room lights (289.14 W/m<sup>2</sup>) and the IR lamp (96.36 W/m<sup>2</sup> each) (Supplementary Fig. 31). Measurement errors are  $0.28 \pm 2.10$  bpm for HR and  $0.28 \pm 1.50\%$  for SpO<sub>2</sub>, respectively. Supplementary Fig. 32 shows changes in SpO<sub>2</sub> and HR while exercising on a stationary bike with the room lights (578.28 W/m<sup>2</sup>) and the IR lamp (289.14 W/m<sup>2</sup> each). Figure 3k shows values of SpO<sub>2</sub> determined once per second from mice in hypoxia and normal states (See Methods and Supplementary Fig. 33), recorded using both a reference mouse oximetry sensor

(MouseSTAT Jr; Kent Scientific; Torrington, CT) and an adaptive PPG sensor, with and without in-sensor computing. This mouse model shows the accuracy of SpO<sub>2</sub> measurement at a low SpO<sub>2</sub> range, near 70 to 80%. This low range SpO<sub>2</sub> damages the brain of human and causes serious diseases such as cyanosis (in the case under the SpO<sub>2</sub> 83%).

### Blue light dosimeter

Blue light penetrates deep into the skin layers, inducing cellular dysfunction and DNA damage<sup>35</sup>. The results can contribute to various cutaneous changes, such as photoaging, hyperpigmentation, and melasma<sup>36,37</sup>. Ideal platforms that offer convenient, real-time access to personalized data on blue light exposure dose could guide behaviors to prevent photo-induced skin damage, while simultaneously harvesting energy from ambient light. Figure 4 introduces a platform that integrates the aPM module with a wireless system that incorporates an accumulation detection module (ADM) for blue-light dosimetry and a BLE SoC for wireless communication<sup>38</sup>. This device, illustrated in Fig. 4a, features soft encapsulation with dual windows to allow ambient light transmission for the ADM and the PV cell (Supplementary Fig. 34), a set of electronic components, and a fPCB that interconnects the aPM module to the ADM configured with a BLE SoC (Fig. 4b; for details, see Methods). The aPM module is identical to that described in the previous section, except with a base battery in this case that has a capacity of 50 mAh. The ADM employs a PD with a peak response at 420 nm (Supplementary Fig. 35a) to convert blue light into a photocurrent that charges a supercapacitor (SC; 11 mF) (Supplementary Fig. 35b). A low-power comparator (LPCOMP) in the BLE SoC monitors the accumulated voltage on the SC ( $V_{SC}$ ). When  $V_{SC}$  exceeds a preset threshold ( $V_{TH} = 0.19$  V, corresponding to a blue light exposure of 1.64 J/cm<sup>2</sup>), the LPCOMP triggers the CPU to exit sleep mode, to measure the voltage via an ADC, to transmit the value to a smartphone, and to discharge the SC via a n-type metal-oxide-semiconductor field-effect transistor (MOSFET) controlled by a GPIO, thus resetting the ADM and returning to sleep mode<sup>28</sup>.

This light-adaptive operation (1) frequently alerts users of their exposure doses during intense irradiation, while entering sleep mode during low or no irradiation and (2) optimizes power consumption based on the detection needs. The sensor consumes 1.89  $\mu$ W of power in sleep mode, and 39.36  $\mu$ W over a runtime of 6.96 s following a wake-up event (Supplementary Fig. 36). The time interval ( $T_{wake}$ ) to wake the sensor from sleep mode varies with light intensity (Fig. 4c), which in turn determines the average current consumption of the sensor<sup>38</sup>. Figure 4d shows the power consumption of the light-adaptive dosimeter and the power generated by the PV cell (Supplementary Fig. 37) under blue light intensities of 0.1, 0.3, 0.5, 1, 1.5, 2, 3, and 4 mW/cm<sup>2</sup> from the solar simulator (A4-LightLine solar simulator, Sciencetech INC.). At the minimum intensity (0.1 mW/cm<sup>2</sup>), the PV cell generates 0.99 mW, which substantially exceeds the operational power requirement of the dosimeter (1.91  $\mu$ W). The excess power charges the PV battery, which supplies energy when ambient light is insufficient for the PV cell to generate adequate photovoltaic output.

Field tests involve continuous measurements of cumulative dose and  $V_{PV}$  as a function of time in Evanston, IL, USA (Fig. 4e, f and Supplementary Fig. 38). Figure 4e and f show measurements from 4 AM to 10 PM on May 9, 2024, under cloudy conditions and on May 11, 2024, under sunny conditions, respectively. A commercial data acquisition (DAQ) device (PowerLab 8/35, ADInstruments) measures  $V_{PV}$  at a sampling rate of 1 Hz. Sensors with and without the aPM module yield identical cumulative doses of 14.40 J/cm<sup>2</sup> under cloudy conditions (Fig. 4e; black) and 200.00 J/cm<sup>2</sup> under sunny conditions (Fig. 4f; black). In sensors without the aPM module,  $V_{PV}$  decreases by  $\sim 0.01$  V under cloudy and sunny conditions. With the aPM module,  $V_{PV}$  increases in both scenarios. Under cloudy conditions, despite a decrease in power generation, the increase in  $T_{wake}$  reduces power consumption, yielding a net increase in  $V_{PV}$  from 3.95 V to 3.99 V

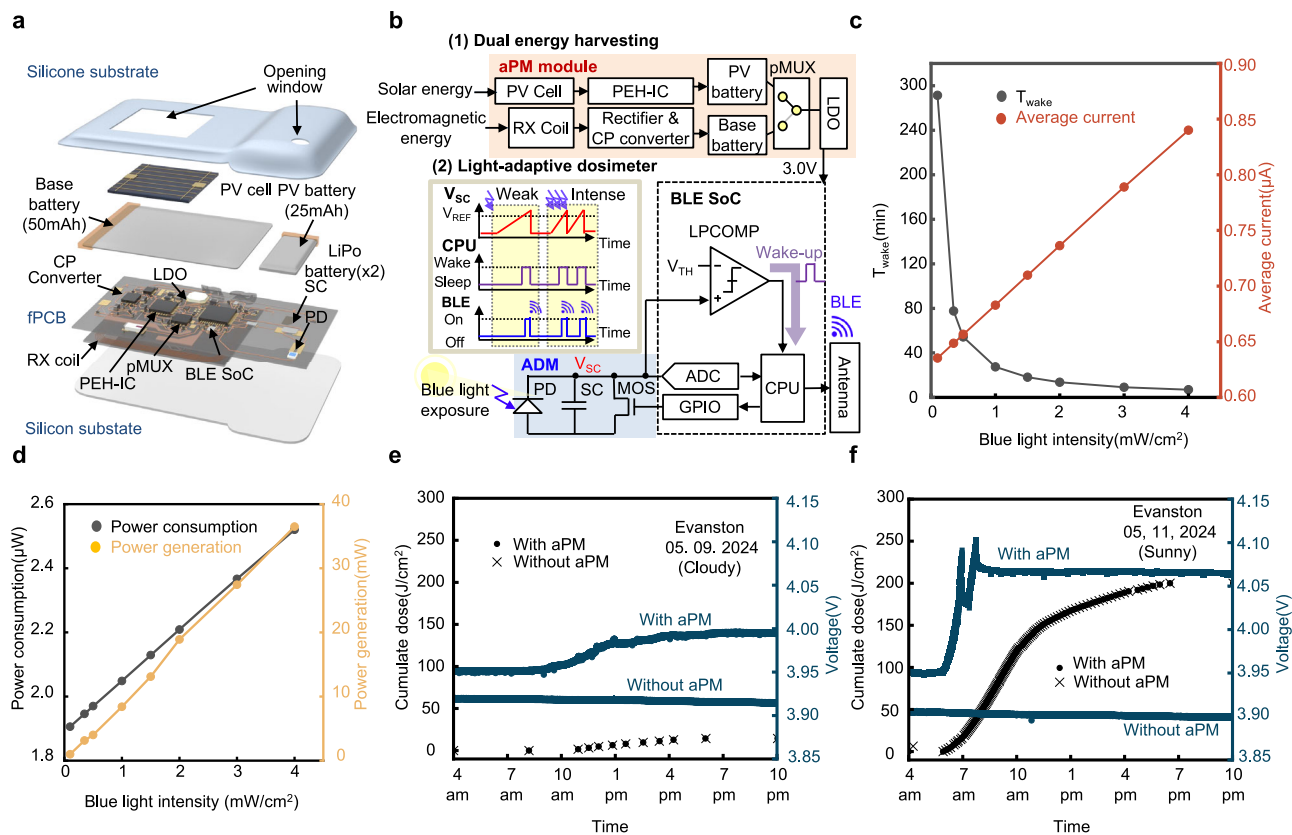


**Fig. 4 | Light-adaptive, power-efficient sensor for blue light dosimetry.**

**a** Exploded view schematic illustration that highlights the PV cell, BLE communication module, an accumulation mode dosimeter, and a pair of LiPo batteries, all attached via an fPCB platform and housed in a silicone encapsulation structure.

**b** Block diagram of the electronics. **c** Average current consumption and T<sub>wake</sub> for continuous use at different blue light intensities. **d** Comparison between the power

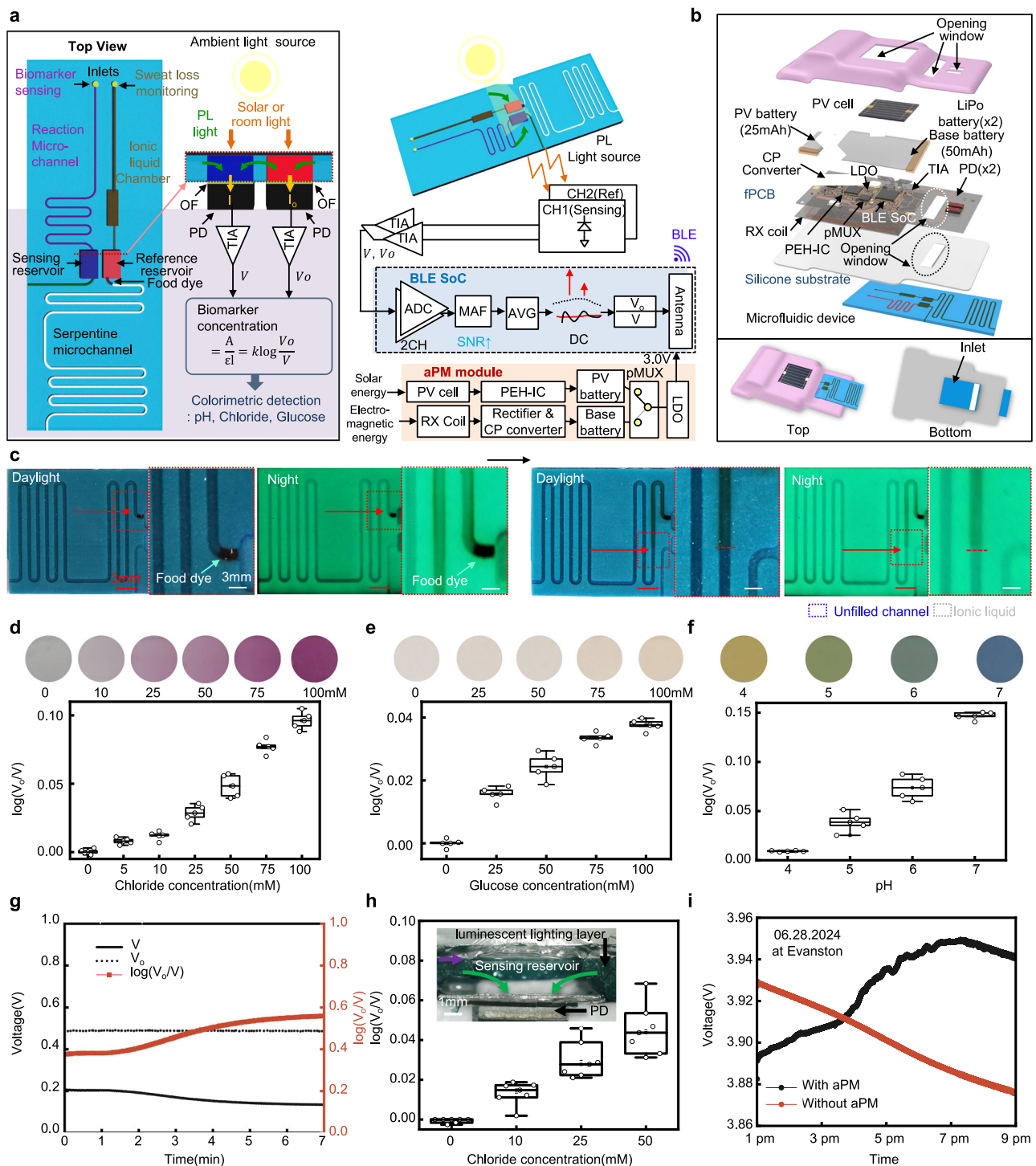
consumption at 3 V operation and power generation from the GaAs triple junction PV cell as a function of blue light intensity provided by a solar simulator, from 0.1 to 4 mW/cm<sup>2</sup>. Results of field studies, showing cumulative dose and battery voltage with and without the aPM module from sunrise to sunset for 18 hours in Evanston at **e**, May 9, 2024 (cloudy weather) and **f**, May 11, 2024 (sunny weather) with the same measuring position.

(Fig. 4e; dark blue). Conversely, sunny conditions, while decreasing T<sub>wake</sub>, increase power generation, leading to an increase in V<sub>PV</sub> from 3.95 V to 4.06 V (Fig. 4f; dark blue). Consequently, in both scenarios, the aPM module facilitates a practical operating lifetime approaching infinity. Furthermore, indoor light is detected by increasing the responsivity, as shown in Supplementary Fig. 39. The blue light sensing module has 10 photodiodes and three SCs in Supplementary Fig. 39a, b. The indoor blue light dosimeter can measure the weak blue light emitted by a computer display (Supplementary Fig. 39c), and instances of excessive blue light exposure can be sent to the user by pop-up alerts or sounds, as shown in Supplementary Movie 1.

### Sweat sensor

Combining light-harvesting schemes and adaptive electronics with microfluidic structures enables power-efficient platforms for wireless sensors of sweat rate, sweat loss and sweat biochemistry. In the example here, a microfluidic platform (Fig. 5a; left) captures sweat from the skin via two separate inlets (diameter: 1.54 mm). Microchannels guide this sweat through structures that allow monitoring of regional sweat rate and total loss, along with sweat pH and concentrations of glucose and chloride. The inlet for monitoring sweat loss connects to an ionic liquid chamber (width: 2 mm, depth: 500 μm, length: 6.2 mm), a reference reservoir (width: 3 mm, length: 4 mm, depth: 500 μm), and a serpentine microchannel (width: 500 μm, depth: 500 μm, length: 170 mm) in series. The ionic liquid (1-ethyl-3-methylimidazolium ethyl sulfate) serves as the reference absorption medium due to its low vapor pressure and absorbance spectrum similar to

sweat in the visible range (400-700 nm; Supplementary Fig. 40)<sup>39</sup>. During sweat collection, pressure from sweat generated by eccrine glands (2.4-2.9 kPa) drives the ionic liquid from the storage chamber into the microchannel. The microchannel is coated with food dye up to 1 mm, beyond which it is uncoated for monitoring loss<sup>39</sup>. Measuring the filling front of the ionic liquid provides a means to quantify the total sweat loss at any given time. The reference reservoir stores the ionic liquid as a reference for accurate biomarker analysis. The inlet for biomarker sensing connects to a reaction microchannel (width: 400 μm, depth: 250 μm, length: 30 mm) pre-loaded with a colorimetric assay, and subsequently to a sensing reservoir (width: 3 mm, length: 4 mm, depth: 500 μm). The assay reacts with target biomarkers in sweat, causing color changes proportional to the concentration. The reaction channel with a volume of approximately 3 μL introduces an acceptable biomarker detection delay of about three minutes at a typical sweat rate of around 1 μL/min. Integrated PDs beneath the reference and the sensing reservoir capture the color changes in the sensing reservoir relative to the reference reservoir, for measurements of biomarker concentrations (Fig. 5a). The PDs configured with optical filters (OF) detect the intensity of light transmitted through reference and sensing reservoirs, defined as I<sub>0</sub> and I, respectively. The optical filters pass the wavelength at which the maximum change in absorbance occurs due to the response of the colorimetric assay (Supplementary Fig. 41)<sup>40</sup>. These wavelengths are 524 nm, 614 nm and 452 nm for chloride, pH, and glucose assays, respectively (Supplementary Fig. 42). Measuring the ratio of light intensities I<sub>0</sub> / I determines the absorbance A = log(I<sub>0</sub>/I) and hence the biomarker concentration (c) by appropriate calibration (for details, see Method and



Supplementary Fig. 43). Sweat sensors with and without in-sensor computing consume 311.10  $\mu$ W and 417.90  $\mu$ W, respectively (Supplementary Fig. 44). The aPM module is identical to that described in the previous section.

An exploded view illustration of the sensor is in Fig. 5b. The top encapsulation layer includes four windows: one for PV cell, two for the assays, and one placed in the middle for assembling microfluidic platform (Supplementary Fig. 45). The fPCB interconnects electronic components for the optical modules and a BLE SoC. The microfluidic part of the sensor comprises a soft silicone elastomer to construct the sweat channels and green phosphorescent fillers, as the PL

component, to serve as light sources in the absence of external illumination (Supplementary Fig. 46). Sweat passes through inlets located at the skin surface (Fig. 5b bottom; right). Reservoirs at the top of the sensor allow light to pass through and reach the PDs below (Fig. 5b bottom; left). Thus, the fPCB and the bottom silicone substrate include windows to the microfluidic component of the system (Supplementary Fig. 45b).

Ionic liquid fills the straight channel and reference reservoir (Supplementary Fig. 47), to allow monitoring of the movement of the front of ionic liquid in the serpentine microchannel as sweat passes into the structure from the inlet, as illustrated in the sequence of

**Fig. 5 | Light-adaptive, power-efficient sensor for sweat rate, sweat loss and sweat biomarker concentrations.** **a** Top view schematic illustration of the microfluidic system and diagram of the mechanism of colorimetric sensing by use of ambient light and block diagram of the electronics and microfluidics. **b** Exploded view schematic illustration that highlights the PV cell, the microfluidic structure, BLE SoC, and the pair of LiPo batteries, all attached via an fPCB platform and housed in a silicone encapsulation structure. **c** Pictures of the sweat sensing part of the system for measuring sweat rate and sweat loss with an arrow that highlights propagation of ionic liquid during operation in daylight (left images) and in the dark (right images). (The red scale bar is 3 mm, and the white scale bar is 3 mm). Pictures that highlight changes in color of the **(d)** chloride **(e)** glucose **(f)** pH assays at different concentrations. The bottom graph shows results of colorimetric sensing based on ambient light (E355998 LED Lamp, Great Eagle), with a log scale representation of the ratio of the photovoltage measured by the sample and reference PDs, at different concentrations ( $n = 5$ ). The minimum and maximum

values (top and bottom lines), the IQR, which spans from the 25th to the 75th percentiles (boundaries of the box), and the median of the dataset (represented by a circle) are shown in the box plots. Whiskers extend to 1.5 times the IQR. **g** The voltage profile of the reference and sensing PDs (black) and log scale representation of the ratio of these two voltages (red) for cases of injection of a 50 mM NaCl solution after a 25 mM NaCl solution under microscopes light (SCW-PGC, Carton Optical Industries). **h** Results of colorimetric sensing of chloride concentration using PL and ratio of photovoltages between the sample and reference PDs at different chloride concentrations in a dark environment ( $n = 7$ ). The top and bottom lines, the boundary of the box, and the circle shape indicate the minimum and maximum results, the IQR within the 25th to the 75th percentiles, and the median. Whiskers extend to 1.5 times the IQR. The inset image shows a cross-sectional illustration of the reservoir with a PL channel structure for operation at night. **i** Dependence of  $V_{PV}$  on time for sensors with and without the aPM module, operated in Evanston, IL.

images in Fig. 5c. As the total volume of the sweat loss monitoring channel is 42.5  $\mu\text{L}$  and the reservoir volume is 6  $\mu\text{L}$ , a total of 48.5  $\mu\text{L}$  of sweat loss can be measured before the ionic liquid is fully depleted. This capacity is more than sufficient to continuously monitor sweat rate for over 90 min in individuals with a moderate sweat rate (0.5  $\mu\text{L}/\text{min}$ ). Once the ionic liquid is depleted, it can be refilled and reused for further measurements (Supplementary Fig. 48). The results for an infusion rate of 2  $\mu\text{L}/\text{min}$  show that the boundary of the ionic liquid, marked with red arrows, moves as expected with the volume of sweat that passes into the channel. The PL (maximum emission wavelength of 520 nm) supports operation in dim lighting or dark conditions. Illuminating the PL material with a UV lamp (365 nm, 4 Watt, EW-97620-00, Cole-Parmer) for 2 min, with the lamp positioned 21.50 cm from the sweat sensor, supports operation for 60 min in the dark (Supplementary Fig. 46). The microfluidic component, positioned above the encapsulation layer, maintains exposure to ambient light, while the inlets adhere to the skin (Fig. 5b; inset). This configuration enables sensor operation via ambient light and energy accumulation within the microchannel for PL light generation under dark conditions.

Figure 5d–f shows chloride and glucose concentrations, and pH levels, derived from the voltage measurements of  $I_{\text{O}}/I$  ( $V_{\text{O}}/V$ ) (Fig. 5d–f; bottom), measured from the sensor under a room light (A190930A LED ramp, Great Eagle; intensity: 23.17  $\text{W}/\text{m}^2$ ), using previously established colorimetric assays<sup>40,41</sup>. As the concentrations of chloride and glucose, and the pH level increase,  $V_{\text{O}}/V$  also increases with a sensitivity of 0.96/ $\mu\text{M}$ , 0.32/ $\mu\text{M}$ , and 0.04/pH, and a limit of detection (LOD) of 3.99 mM, 22.73 mM, and 2.68 pH, respectively (for details, see Supplementary Figs. 49, 50, Supplementary Note 8 and Methods). The WST-8–based glucose assay, which is less susceptible to degradation or denaturation by light and oxygen, offers stable glucose sensing capability within the physiologically relevant range.

The reaction microchannel design allows complete colorimetric reactions before sweat enters the sensing reservoir. When designing a sweat biomarker sensing channel, it is imperative to account for both the sweat rate and the biomarker reaction kinetics. The residence time of sweat within a fixed-volume reaction channel is governed by the sweat rate, critically influencing the extent to which analyte–reagent reactions can be fully completed. For accurate analyses, the reaction channel must be designed so that the residence time exceeds the required reaction time even in individuals with elevated sweat production. Finite element analysis (FEA) simulations of acid chloranilate ion diffusion within the microfluidic channel (width: 400  $\mu\text{m}$ , depth: 250  $\mu\text{m}$ ) demonstrate that, even at higher flow rates, the convection–diffusion profile allows sufficient residence time for chloride sensing (Supplementary Fig. 51)<sup>42</sup>. The reaction times for chloride, glucose, and pH detection are approximately 10 min, 5 min, and 3 min, respectively<sup>41</sup>. Consequently, a 30 mm channel length ensures that sweat remains in contact with the reagents for at least 10 min, accommodating the longest reaction time required for

chloride detection. The results confirm that this design facilitates complete diffusion and reaction for all three analytes, regardless of individual differences in sweat rate (for further details, see Methods). Figure 5g demonstrates the operation, through measurements initiated with 25 mM NaCl solution injected into the reaction channel (length: 30 mm), followed by a 50 mM solution. This increase in concentration increases the absorption of green light (530 nm), decreasing the value of  $V$  while  $V_{\text{O}}$  remains constant, thereby increasing the ratio  $V_{\text{O}}/V$  (red). Figure 5h demonstrates chloride sensing under PL illumination, yielding a slightly reduced sensitivity of 0.90/ $\mu\text{M}$  and increased LOD of 11 mM, compared to room light illumination (intensity: 23.17  $\text{W}/\text{m}^2$ ) in Fig. 5d.

A field study defines the variation of  $V_{PV}$  in sensors with and without the aPM module, demonstrating the aPM capability (Fig. 5i). Over a 8 h period from 1 PM to 9 PM, the value of  $V_{PV}$  without the aPM module decreases from 3.93 V to 3.87 V, while with the aPM module it increases from 3.89 V to 3.95 V. With the aPM module,  $V_{PV}$  increases most significantly from 1 PM to 7 PM, corresponding to the period of significant power generation by the PV cell.

### Light-adaptive multimodal sensor

Figure 6 shows an integrated sensing platform that combines previously described modalities with an additional temperature sensing capability. The sensor, illustrated in Fig. 6a and b, consists of a PL layer, a microfluidic channel, top/bottom encapsulation layers, a set of electronic components and a fPCB. (Supplementary Fig. 52 and Note 9) The weight of the multimodal sensor is comparable to that of previously reported lightweight multimodal sensors (Table S2). The integration of smaller-sized batteries into the universal energy harvesting system enables further reduction in the overall device weight. Temperature sensing uses a voltage divider with a negative temperature coefficient (NTC) thermistor and a 220 k $\Omega$  resistor<sup>43</sup>. Temperature fluctuations induce resistance changes in the NTC, resulting in voltage variations measured by the ADC in the BLE SoC for skin temperature conversion. Supplementary Fig. 53 shows measurement results from the sensor placed in an oven (LH 1.5, Associated Environmental System), across a range from 10  $^{\circ}\text{C}$  to 50  $^{\circ}\text{C}$ , with comparison to those from a commercial temperature sensor. To ensure that both devices can firmly attach to the forearm and neck, FEA defines the normal stress distribution on the skin surface. The maximum principal strain in the Ecoflex layer of PPG sensor (Supplementary Fig. 54a) and multimodal sensor (Supplementary Fig. 54b) is 10%, which is well below its fracture strain of 100% (Supplementary Fig. 55a). The maximum normal stress of the PPG sensor (Supplementary Fig. 54c) and the multimodal sensor (Supplementary Fig. 54d) at the skin surface is below 5 kPa which is lower than the tensile strength of 10 kPa of our adhesives (Supplementary Fig. 55b). In addition, this maximum normal stress is significantly below the normal threshold for sensation (~20 kPa)<sup>44–46</sup> and is on the same order of threshold for sensation in extreme skin

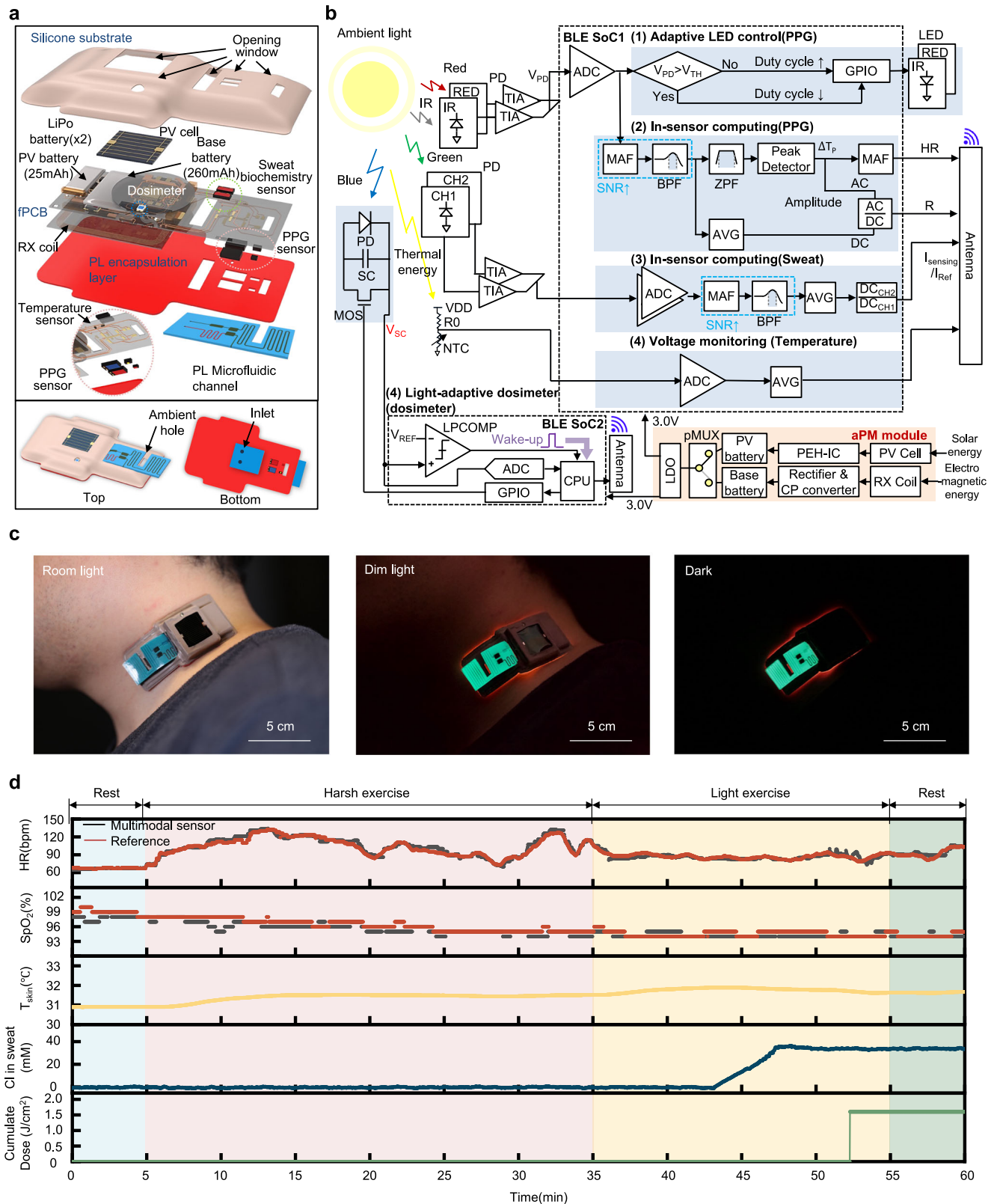


**Fig. 6 | Light-adaptive, power-efficient multifunctional sensor. a** Exploded view schematic illustration that highlights all of the components featured in the other sensors, with the addition of a temperature sensor. **b** Block diagram of the electronics. **c** Images of the sensor on the neck with under room light, dim light, and dark environments. **d** On-body test results for measuring HR, SpO<sub>2</sub>, skin temperature, sweat chloride (Cl) concentration, and blue light dosimetry during exercise (Red: reference results, black: results from the multimodal sensor).

sensitivity ( $\sim 2$  kPa)<sup>44,45</sup>. These results demonstrate that both devices can effectively conform to the body without device failure nor constraining movement. Furthermore, the energy harvesting system can be applied with a broad range of photovoltaic cells and batteries. Use of arrays of microscale components as alternatives to the cells and batteries implemented here can improve the flexibility of these sensors<sup>47,48</sup>. In addition, as illustrated in Supplementary Fig. 56, deformations between the sweat channel and the electronic module near the insertion site facilitate conformal contact of both the PPG sensor module and the sweat channel inlet with the skin<sup>44</sup>.

The current consumption of the multimodal sensor with and without in-sensor computing is 893.28  $\mu$ W and 921.39  $\mu$ W, respectively, with all LEDs inactive under daylight conditions (intensity: 578.28 W/m<sup>2</sup>; Supplementary Fig. 57). The power consumption decreases as expected with increasing wireless data transmission interval from 1 min (466.31  $\mu$ A), to 2 min (431.25  $\mu$ A), and 5 min (419.03  $\mu$ A) (Supplementary Fig. 58). At 5 min, the multimodal sensor can operate for 22 h 56 min with PV harvesting without electromagnetic harvesting during indoor activity. The maximum operating duration of the multimodal sensor, at a sampling rate of 1 Hz, is approximately 9 days using only photovoltaic energy harvesting without electromagnetic harvesting as shown in Supplementary Fig. 59.

Figure 6c shows optical images of the sensor attached to the neck in three different lighting environments: bright and dim room light and dark environments. The microfluidic component and the bottom encapsulation layer emit green and red PL, respectively, in dim and dark environments. Figure 6d shows simultaneous measurements of HR, SpO<sub>2</sub>, skin temperature ( $T_{\text{skin}}$ ), sweat chloride concentration (all at 1 Hz), and blue light dosimetry from a sensor attached to the neck of a healthy subject during indoor exercise under room light (intensity: 289.14 W/m<sup>2</sup>); (Supplementary Note 9 and Supplementary Fig. 60). Supplementary Fig. 61 shows the BA plot for HR and SpO<sub>2</sub> of Fig. 6d. The deviation of SpO<sub>2</sub> from the reference results from motion artifacts<sup>49,50</sup>.

## Discussion

The electronically adaptive schemes and light-harvesting approaches reported here, together with capabilities for in-sensor data analytics, dramatically reduce the power requirements for sensors that rely on optical approaches in skin-interfaced medical monitors. Detailed studies across multiple sensor modalities reveal the key features of these approaches, as well as the advantages and disadvantages of each. Many of the same electronics strategies apply to other methods for energy harvesting, such as those based on mechanical motions or thermal gradients, in ways that are also compatible with the optical schemes presented here. Broad, multimodal schemes will likely be essential for practical applications, due to their ability not only to enhance the overall harvesting capacity but also to mitigate unavoidable intermittencies. Additional work in this direction promises to lead to further improvements in continuous medical monitoring technologies, with broad implications for efficient management of human health.

## Methods

### Fabrication of the electronics

Flexible printed circuit boards (fPCBs; PCBway) with a thickness of the 0.13 mm served as the basis for the sensors. A small amount of soldering paste (SMDLTLFP10T5, Chip Quik) placed on the Au electrode pads of the fPCB enabled manual integration of surface-mounted components using a needle for manipulation. The paste bonded and electrically connected these components to the fPCB by heating at 180 °C for 10 s, to melt the metal particles (Sn<sub>42</sub>/Bi<sub>57.6</sub>/Ag<sub>0.4</sub>), and to solidify the joint to the fPCB. The components included: BLE SoC (nRF52832, Nordic Semiconductor), BLE antenna (2450AT18A100, Johanson Technology), InGaP, GaAs, and InGaAs triple junction PV cell (TSC-E-3J-AA-4.00-T0, Micolink), diode rectifier (BAS40XY, Nexperia),

PEH-IC (AEM10941, e-peas), CP converter (LTC3255, Analog Device), pMUX (TPS2115ADRBT, Texas Instruments), and a LDO regulator (TCR3UM33A, Toshiba). In the different components for each sensor, the PPG sensor includes red (LXZI-PH01, Lumileds) and IR (VSMB1940ITX01, Vishay Semiconductor Opto Division) LEDs, PDs with peak wavelengths at 620 nm (SFH2240, ams-OSRAM USA INC.) and 940 nm (SFH2200, ams-OSRAM USA INC), TIA (ADA4505, Analog Devices). The PPG sensor comprises 25 mAh (LP191320) and 260 mAh (LP452525) LiPo batteries. The dosimeter used a blue PD (PB01-LXZ1, Lumileds), a capacitor (CPH3225A, Seiko Instruments), and N-MOSFET (CSD17381F4, Texas Instruments), with 25 mAh (LP191320) and 50 mAh (LP103035) LiPo batteries. The sweat sensor included two red PDs with a peak wavelength at 620 nm (SFH2716, ams-OSRAM USA INC), op-amp (ADA4505, Analog Devices), with 25 mAh (LP191320) and 50 mAh (LP103035) LiPo batteries. The multimodal sensor includes 5 PDs: a red PD (SFH2240, ams-OSRAM USA INC.), an IR PD (SFH2200, ams-OSRAM USA INC.), a blue PD (PB01-LXZ1, Lumileds), and two red PDs (SFH2716, ams-OSRAM USA INC.). The system also included red (LXZI-PH01, Lumileds) and IR (VSMB1940ITX01, Vishay Semiconductor Opto Division) LEDs, a capacitor (CPH3225A, Seiko Instruments), N-MOSFET (CSD17381F4, Texas Instruments), and two TIA (ADA4505, Analog Devices). The sensor used 25 mAh (LP191320, LiPol Battery) and 260 mAh (LP452525, LiPol Battery) LiP batteries. Soft silicone materials, including Ecoflex (00-30, Smooth-on) and poly(dimethylsiloxane) (PDMS) (Sylgard 184, Dow Corning) formed encapsulating structures, using molding procedures described elsewhere.

### Encapsulation process

The molds for the encapsulating structures used aluminum blocks (McMaster-Carr) processed using a three-axis milling machine (Modela Pro II MDX 540, Roland DGA). Soft silicone materials (Ecoflex 00-30, Smooth-on) mixed with 9% white silicone dye (Silc Pig, Smooth-on) and 1% of another silicone dye formed the top encapsulation layer (PPG sensor with length of 61.9 mm and width of 41.0 mm - blue; blue light dosimeter with length of 55.0 mm and width of 44.7 mm - cyan; sweat sensor with length of 72.0 mm and width of 38.1 mm; and multimodal sensor with length of 78.7 mm and width of 35.8 mm - brown). Compression molding formed the top encapsulation layer as a pressure of 2000 lbs and a temperature of 150 °C by hot pressing (3895.4PL0000, Carver). Spin coating of the silicone material at a speed of 500 rpm for 30 s formed the bottom encapsulation layer (0.4 mm thickness). The bottom encapsulation layers of the sweat sensor and dosimeter used silicone materials made by mixing Ecoflex 00-30 and 10% white silicone dye (Silc Pig, Smooth-on) with a thickness of 0.71 mm. The bottom encapsulation layer of the PPG and multimodal sensor used Ecoflex 00-30 mixed with the same weight of a phosphorescent filler (Glow worm red, Smooth-on) with a thickness of 0.71 mm. In all cases, curing occurred on a hot plate at 60 °C for 2 h. Laser ablation with a CO<sub>2</sub> laser (Universal Laser system) formed windows for the PDs, LEDs, ambient light, and sweat inlets and outlets. Encapsulation involved placing the top layer on the aluminum mold, placing the fPCB with electronic components and batteries inside, and aligning the PDs, openings, and PV cells to windows. PDMS filled the vacant volume, to allow bonding to the bottom layer by curing the PDMS. Curing for 1 h at 60 °C in an oven, followed by cutting excess material away from the perimeter using a CO<sub>2</sub> laser completed the process.

### Fabrication of transparent PPG sensor

The transparent fPCB incorporated a polyethylene terephthalate (PET) substrate with a thickness of 0.2 mm, purchased from PCBWAY. This transparent PPG sensor used the same electronic components and circuit design as the non-transparent version. The top encapsulation mold used aluminum blocks (McMaster-Carr) and processed using a milling machine (Model Pro II MDX 540, Roland DGA) (length of 61.9 mm and width of 41.0 mm). Uncured PDMS (Sylgard 184, Dow

Corning) was filled in the mold prior to hot pressing and thermal curing for the top encapsulation layer. The bottom encapsulation layer used Ecoflex 00-30(60 g) mixed with a phosphorescent filler(60 g) (Glow worm red, Smooth-on), in a thickness of 0.71 mm. Thermal curing occurred on a hot plate at 60 °C for 2 h for the bottom encapsulation layer. Ablation with a CO<sub>2</sub> laser (Universal Laser system) defined windows. Complete encapsulation involved placing the top encapsulation layer and the fPCB with electronic components, batteries, PV cells, and the bottom encapsulation layer in the top encapsulation mold and filling the vacant space via PDMS. Curing for 3 h at 60 °C in an oven, followed by laser ablation with a CO<sub>2</sub> laser to define the outline, completed the process.

### RX coil design

The RX coil consisted of gold features patterned on a PI substrate, with dimensions of 200 μm width, 200 μm spacing, and 6 turns. The theoretical inductance is 2.62 μH, and the matching capacitor is 45 pF for operation at 13.56 MHz.

### On-body tests with human participants

The experimental protocols for tests of the PPG and multimodal sensor were approved by the Institutional Review Board of Northwestern University (STU00220375). Participants provided consents prior to any testing. Healthy adult volunteers (aged 25–36 years, 16 male and 2 female with normal SpO<sub>2</sub> > 95%, Table S1) performed breath holds, breathed air with controlled oxygen concentrations, and exercised to modulate the HR and SpO<sub>2</sub> levels, as described by the study safety guidelines. The testing location was cleaned with an alcohol swab, and the contamination effect on the properties of the PPG was removed. The detailed protocols appear in the following.

**Breath hold.** The measurements involved sensors attached to various locations, such as the fingers, ears, neck, and toes. Comparisons examined SpO<sub>2</sub> and HR measured from the light adaptive PPG sensor and from a reference system (Dash-3000, GE) at the same time during 1 to 3 min of normal breathing, followed by a breath hold for between 30 s and 1.5 min, followed by resumption of normal breathing for 1 to 2 mins until stabilization of SpO<sub>2</sub> for another 2 min. The reference HR and SpO<sub>2</sub> were recorded from the outer camera of the cell phone (iPhone 14 pro-Max, Apple), and red/IR PPG signals or sensor computing HR/SpO<sub>2</sub> data were recorded from the outer cell phone (Galaxy S10, Samsung electronics).

**Oxygen concentration control.** Measurements under controlled oxygen levels involved sensors attached to the index finger or neck. After measuring HR and SpO<sub>2</sub> at an oxygen concentration of 20% or higher for 2 mins with the sensor and a reference system (Dash 3000, GE), a hypoxia system (Sierra 300, Hypoxia Inc.) was engaged to decrease the administered oxygen concentration to ~13%. Measurements of HR and SpO<sub>2</sub> continued with lowering of the oxygen concentration until the SpO<sub>2</sub> reached 85%. The system then increased the oxygen concentration to 20% or higher until the SpO<sub>2</sub> reached 95% or higher. Monitoring of HR and SpO<sub>2</sub> then continued for another 2 min. The data recording method is the same as the breath-hold method.

**Physical exercise.** The measurements involved mounting the sensor on the neck using a medical adhesive (Tegaderm, 3 M). A finger-type oximeter (Dash3000, GE) attached to a finger served as a reference for HR and SpO<sub>2</sub>. The conditions included 5 min of normal breathing on a stationary bicycle without movement, followed by cycling for 20–50 min at different intensity levels, and then resting with normal breathing for 5 min. Wireless transmission of HR, SpO<sub>2</sub>, skin temperature, chloride concentration in sweat and exposure dose to blue light passed data to cell phones and a laptop.

### Power consumption of the App

Connecting the cell phone to the laptop computer allowed measurements of power consumption of the app with the 'Dumpsys' tool in the Android studio through evaluations of the battery discharging rate in 'batterystats.' The average power was measured for 5 min, three separate times. The base current consumption was 75.63 μA, without communication with the PPG sensor. Comparisons of consumption with or without in-sensor computing during communication with the sensor involved the subtraction of this base value.

### Animal tests of the PPG sensor

C57BL/6 or Balb/c mice (weight 25–30 g; age 20–24 weeks) were purchased from Jackson Laboratory (Bar Harbor, ME) and Charles River (Wilmington, MA) respectively. The animals were kept on a 12 h light-dark cycle in a temperature-controlled room. The experimental procedures were approved by the Animal Care and Use Committee of Northwestern University and conformed to the Guide for the Care and Use of Laboratory Animals (Institute for Laboratory Animal Research, National Academy of Sciences, ed. 8, 2011). Mice were anesthetized with an intraperitoneal injection of Ketamine/Xylazine (80/5 mg/kg). Mice were placed in the supine position on a warming platform. A nose cone was used to provide supplemental 100% oxygen (normal state). Varying levels of oxygenation was achieved by removing supplemental oxygen intermittently for hypoxia states. Mice were maintained at approximately 37 °C on a heating pad with 45–65% humidity. The animal's hair was removed from the surgical site with hair removal cream NAIR after shaving. The reference oximeter probe was placed over the chest or foot of the mouse and secured with tape (300926, Delne). Peripheral blood oxygen saturation was monitored throughout the experiment using a commercial PPG sensor system as a reference oximetry sensor (MouseSTAT Jr; Kent Scientific; Torrington, CT) under room light (E355998 LED Lamp, Great Eagle) or/and IR lamp (CM-IRP6-850, CMVision). The reference SpO<sub>2</sub> were recorded from the camera of a cell phone (iphone 14 pro Max, Apple). The parylene coated light adaptive PPG sensor was placed on the neck of the mouse and fixed with tape (300926, Deline). The red/IR PPG signals (sampling rate: 100 Hz) and in-sensor computed SpO<sub>2</sub> results (sampling rate: 1 Hz) are measured from the outer of the cell phone (Galaxy S10, Samsung Electronics). At first, 100% oxygen is given to the mouse for the initial two minutes, and the oxygen gas is removed for 4 min to induce a hypoxia state. After 4 min in the hypoxia, 100% oxygen is reintroduced to the mouse for 4 min. The sequence is repeated for 1-2 cycles.

### Measurements of power consumption

The voltage and ground electrodes of the sensor are connected to the voltage and ground lines of a power profiler kit (nRF-PPK2 power profile kit, Nordic). A laptop computer with Nordic software (nRF connect for Desktop 4.4.1, Nordic) measured the average current consumption of sensors at an operating voltage of 3V for different measuring times from 10 s to 24 h by measuring current consumption (sampling rate: 1000 Hz).

### Measurements of photovoltage with a blue PD

Performance evaluations use a commercial blue light radiometer (9.4 Blue Light, Solarmeter) to measure the reference exposure intensity from a blue lamp (ZC-10S, NEEWER). The sunlight intensities were measured from a light meter (20250-00, Digi-sense). The photovoltage of the blue light PDs (PB01-LXZ1) was measured from the multi-voltage data logger system (PowerLab 8/35, AD Instruments), depending on the blue light intensities from the blue light lamp in the dark room.

### Fabrication of a sweat microfluidic channel

For the PL bottom channel layer of the sweat microfluidic channel, a 3D printer (Formlabs) defined the molds from a clear resin, cross-linked under UV light for 15 min at room temperature and coated

with parylene by chemical vapor deposition (SCS Labcoter 2 Parylene Deposition System, Specialty Coating System, IN). The silicone elastomer base (Sylgard 184, Dow Corning), crosslinker, and PL filler (glow worm bold blue, Smooth-On, Inc.), mixed with a 1:0.1:1 weight ratio was poured onto the upper and lower mold and placed in a vacuum desiccator for degassing for 20 min. Assembling the upper and lower molds with clips, preceded curing at 75 °C in an oven for 1 day. For the preparation of the transparent top layer, a bilayer structure consisting of an adhesive layer and a matrix layer was fabricated. Initially, the adhesive layer was fabricated by mixing a silicone base and a curing agent with a weight ratio of 60:1. This mixture was then coated onto a polymethylmethacrylate (PMMA, thickness 20 μm) on a silicon wafer using spin coating with 500 rpm for 30 s. It was then cured on a hot plate at 75 °C for 2 h. Next, a solution was prepared to fabricate the matrix layer on top of the adhesive layer by mixing a silicone base and a curing agent with a weight ratio of 10:1. This solution was spin-coated onto the adhesive layer at 500 rpm for 30 seconds. The film was then cured in an oven at 75 °C for 6 h. Before attaching the top and bottom layers, the colorimetric assay and food dye (Violet and green color, Nomeca) was loaded into the continuous channel and serpentine micro-channel, respectively. The assays for chloride, pH, and glucose were prepared according to the following:

**Chloride.** 50 mg of silver chlorinate (GreenRoom Board, North Carolina, USA) mixed with 200 μL of 2% w/w Poly(2-hydroxyethyl methacrylate) (PHEMA) methanol solution formed the basis for the chloride assay. Casting this solution into the 30 mm-long channel between an inlet and a reservoir and drying it in a desiccator for 5 min completed the assay immobilization.

**pH.** The pH indicator consisted of 10 mg bromocresol purple (Sigma-Aldrich, MO, USA) and 10 mg bromocresol green (Sigma-Aldrich, MO, USA) mixed into a solution of 0.04 wt% of bromothymol blue in 100 mL (Sigma-Aldrich, MO, USA). Casting onto a filter paper and drying in a desiccator for 1 h completed the assay immobilization.

**Glucose.** Abcam, Inc supplied the glucose assay kit (ab102517). A buffer mixed with glucose substrate and glucose enzyme were cast into the reservoir and dried at room temperature in a desiccator to immobilize the assay.

Following loading each of these assays and manually attaching the top and bottom layers after exposure plasma treatment, heating at 75 °C in an oven for one day completed the fabrication. Ionic liquid (1-ethyl-3-methylimidazolium ethyl sulfate, Sigma-Aldrich) injected into the inlet filled the two reservoirs (an ionic liquid reservoir and a reference photovoltage measuring reservoir) in the reference channel part of the system.

### Colorimetric system of the sweat sensor

The OS module and two PDs followed by the TIAs, convert  $I_0$  and  $I$  into voltages,  $V_0$  and  $V$ , as given by Voltage [mV] =  $0.44 \times$  Light Intensity [Lux] - 0.49 (Supplementary Fig. 43). In the BLE SoC (Fig. 5a; right), 2-channel ADCs digitize the values of  $V_0$  and  $V$  at a sampling rate of 100 Hz. The in-sensor computing system removes noise via a MAF and AVG process, calculates the voltage ratio,  $V_0/V$ , and transmits the ratio to the smartphone. A customized App calculates  $c$  from the ratio by  $c = k \times \log(V_0/V)$  where  $k$  is a calibration coefficient.

### Benchtop studies of the sweat sensor

Reaction of solutions of chloride, pH, and glucose with the respective assays served as standards for measurements of absorbance. Chloride standards involved mixing of immobilized chloride assays and NaCl solutions with concentrations of 0, 5, 10, 25, 50, 75, and 100 mM for 2 h. pH standards involved casting of buffer solutions (Thermo Fisher) with

pH of 3, 4, 5, 6, and 7 and assay solutions at a volume ratio of 10:1 on cellulose acetate membrane filter paper (0.2 μm pore size filter, CA0247100, Sterlitech) followed by drying for 2 h. The glucose standards involved forming glucose solutions with concentrations of 0, 25, 50, 75, and 100 mM by mixing 100 mM glucose solutions (ab102517, Abcam) with a buffer solution. The glucose assay solutions were prepared by mixing the glucose buffer, substrates, and enzyme solutions at a volume ratio of 46:2:2 for 2 h. Finally, the glucose solutions and the glucose assay solutions were mixed with a volume ratio of 1:1 for 30 min.

The Nanodrop system served as an instrument for measuring the absorbance from 2.2 μL volumes of samples, across a range of wavelengths from 300 to 800 nm. For characterization of the sweat monitoring sensor, ionic liquid filled the reference channel. A syringe pump (Havard apparatus) delivered solutions into the system at different flow rates to the sample channel. Activation of a room light lamp (E355998 LED Lamp, Great Eagle or SCW-PGC, Carton Optical Industries) in a dark environment provided 47 klux illumination to approximate lower daylight conditions. Experiments involved positioning the two reservoirs of the sweat sensor below a room light, while the sensor transmitted two  $V_0$  and  $V$  results to a cell phone while injecting the solutions from the syringe pump into the sample channel. Demonstrations of the PL mode of operation began with positioning the sensor under a UV lamp (345 nm, EW-97620-00, Cole-Parmer) for 2 min in an otherwise dark room. The sensor was operated for 2 min after blocking the UV light. The limit of detection (LOD) follows from  $LOD = \frac{3.3\sigma}{S}$  here  $\sigma$  is the standard deviation of the response and  $S$  is the slope of the calibration curve. The slope also corresponds to the sensitivity. Linear extrapolations were conducted based on Fig. 4f, g, using the OriginLab data analysis tool to obtain the standard deviation and slope. For continuous monitoring, the measurement started 20 min (time for sweat to reach the sensing receptor) after the sweat injections and continued until 40 min (time for the chloride ion assay to be depleted) later.

### Simulation

**Computing  $q_2$  using diffusion theory.** For a point light source with power  $P$  on the flat tissue surface, the intensity  $I$  received by a PD located on the same surface at a distance  $r$  from the source depends on the absorption coefficient  $\mu_a$ , the reduced scattering coefficient  $\mu'_s$ , and refractive index  $n$  of the tissue. According to diffusion theory, the analytical solution is<sup>51</sup>

$$I = 0.306P \left[ \frac{l e^{-\mu_e l_r} (1 + \mu_e l_r)}{4\pi l_r^3} + \frac{(l + 2l_b) e^{-\mu_e l_i} (1 + \mu_e l_i)}{4\pi l_i^3} \right] + 0.118P \left( \frac{e^{-\mu_e l_r}}{4\pi D l_r} - \frac{e^{-\mu_e l_i}}{4\pi D l_i} \right) \quad (1)$$

where  $l_b = 5.897D$ . The factors 5.897, together with 0.306 and 0.118 depend on the refractive index, which is 1.4 in our case. Other parameters are  $l = \frac{1}{\mu_a + \mu'_s}$ ,  $D = l/3$ ,  $l_r = \sqrt{r^2 + l^2}$  and  $l_i = \sqrt{r^2 + (l + 2l_b)^2}$ ,  $\mu_e = \sqrt{3\mu_a(\mu_a + \mu'_s)}$ .

The red LED has lateral dimensions of 0.1 cm × 0.1 cm and is divided into a 50 × 50 array of small sources, each treated as a point source. Similarly, the IR LED measures 0.038 cm × 0.034 cm and is divided into an array of 38 × 34 smaller sources. The window to expose the skin to ambient light measures 0.22 cm × 0.81 cm and is divided into an array of 22 × 81 smaller sources. The photodetector measures 0.285 cm × 0.285 cm and is divided into an array of 57 × 57 smaller detectors. The detected power of each detector corresponds to the product of the intensity at its center (Eq. (1)) and its area. By summing the contributions from all sources and the detected intensities from all detectors, the total received power across the entire detector from the

full source is determined. Further partitioning of the detectors and sources does not alter the results.

The light sources emit radiation with characteristic wavelength distributions. Likewise, the detectors have sensitivities that depend on wavelengths. The product of the intensity and the sensitivity integrated across all wavelengths determines the total received power. To determine the received power at different wavelengths, Eq.(1) requires the values of  $\mu_a$  and  $\mu'_s$  across those wavelengths. Tissue absorption primarily stems from hemoglobin, both oxidized and deoxygenated. As blood constitutes approximately 5% of body volume<sup>52</sup>, with a hemoglobin concentration of 150 g/L<sup>53</sup> and a molar mass of 64500 g/mol, the total concentration of hemoglobin in tissue, denoted as  $c$ , is  $1.16 \times 10^{-4}$  mol/L. Venous blood accounts for approximately 75% of the total blood volume<sup>52</sup>, with an SvO<sub>2</sub> of 60%<sup>54</sup>. The overall absorption of blood is thus:

$$\mu_a = 0.75c \left[ SvO_2 \varepsilon_{HbO_2} + (1 - SvO_2) \varepsilon_{Hb} \right] + 0.25c \left[ SpO_2 \varepsilon_{HbO_2} + (1 - SpO_2) \varepsilon_{Hb} \right] \quad (2)$$

The analysis disregards the differences between SpO<sub>2</sub> and SaO<sub>2</sub>. The molar absorption coefficients of oxidized ( $\varepsilon_{HbO_2}$ ) and deoxygenated ( $\varepsilon_{Hb}$ ) hemoglobin can be found in reference [<https://omlc.org/spectra/hemoglobin/>], facilitating the derivation of  $\mu_a$  as a function of wavelength. Simulations of pulsatile blood flow involve introduction of 5% variation in arterial blood volume to calculate  $\mu_a$ . The reduced scattering coefficient of the tissue is approximately  $\mu'_s = 18 \times (1 - 6.3 \times 10^{-4} \lambda) cm^{-1}$ <sup>55</sup>, where  $\lambda$  is the wavelength in nm.

**Propagation of light from PL in tissue.** The diffusion theory captures the propagation of light from photoluminescence within the tissue. The PL region is divided into  $0.04 \times 0.04$  cm<sup>2</sup>, with each square modeled as a point source. On the top surface, apart from the windows for the ambient, the LEDs and the PDs, all regions emit an equal amount of light. The emitted light from PL has a wavelength of 620 nm. The absorption coefficient is adopted as Eq. (2) when SpO<sub>2</sub> is 90%. The reduced scattering coefficient of the tissue is also  $\mu'_s = 18 \times (1 - 6.3 \times 10^{-4} \lambda) cm^{-1}$ . The total PL power in Fig. 3f is 1 W.

**Computed intensity distributions associated with combined light sources.** Diffusion theory defines the distribution of intensity associated with combined illumination by the LEDs, ambient light and PL light. The intensity of the combined source of each pixel is then determined by the weighted sum of three sources: LED, ambient light from the window, and PL. The weight for each source is based on its total irradiation power.

**Convection-diffusion equation in the sweat channel.** The simulations employ a sweat rate of 2  $\mu$ L/min, representing the upper limit of the physiological range for the sensor geometry with a 10 mm<sup>2</sup> sweat collection area. A convection-diffusion equation describes the concentration profile of acid chloranilate ion within a channel characterized by length  $l = 30$  mm, width  $b = 0.4$  mm, and height  $h = 0.2$  mm. The channel filling time is calculated to be 1.2 minutes. The density and viscosity of the water are 1000 kg/m<sup>3</sup> and 0.001 Pa/s, respectively. Given a maximum average flow velocity of  $4.17 \times 10^{-4}$  m/s, the maximum Reynolds number is  $0.083 \ll 1$ . Consequently, the creeping flow model in COMSOL 6.0 can determine the steady velocity profile of the water, denoted as  $\mathbf{v}(x, y)$ . The convection-diffusion equation governing the concentration of the chloranilate ion  $c$  is

$$-D \nabla^2 c + \mathbf{v} \cdot \nabla c = 0 \quad (3)$$

where  $D = 1 \times 10^{-9}$  m<sup>2</sup>/s is the diffusivity in water. At the inlet ( $z = 0$ ), the concentration is zero. At the bottom boundary ( $x = 0$ ), the reaction is

rapid, resulting in the acid chloranilate ion reaching its maximum concentration  $c_0$ . At all other four boundaries, the diffusive flux is zero.

**Finite element analysis (FEA) for mechanical deformation.** The commercial software ABAQUS (version 2023) is utilized to evaluate the device conformability to the forearm and neck. The PDMS and Ecoflex substrates were modeled using the incompressible Neo-Hookean hyperelastic constitutive model. The material parameters, measured from our experiments were  $C_1 = 859.5$  kPa for PDMS (10:1),  $C_1 = 46.27$  kPa for Ecoflex with microparticles, and  $C_1 = 45.28$  kPa for Ecoflex with brown dye. These values were obtained through experimental mechanical testing (Supplementary Fig. 55a). The radius of curvature of the forearm and neck was approximated as 50 mm and was then modeled as a cylinder using the incompressible Neo-Hookean hyperelastic constitutive model, with  $C_1 = 21.67$  kPa<sup>56,57</sup>. The electronic components have Young's modulus of 1500 MPa<sup>58</sup>, which is significantly higher than that of PDMS and Ecoflex. It was verified that further increases in the modulus did not affect the results. A non-penetration contact condition was applied between the device and the skin. Device geometries were derived from experimental prototypes and incorporated fillet features with a 0.1 mm radius at critical junctions. To ensure proper attachment, an initial pressure was applied to the device on the surface of the body, and the device remained adhered after contact. Once fully adhered, the external force was removed, and the adhesive stress was analyzed to assess its conformability to the human body. The simulations employed tetrahedral elements (C3D8RH), with a total of 4,053 elements for PPG sensor and 9,762 elements for the Multimodal sensor. Geometrical nonlinearity was considered in all simulations, and mesh convergence was ensured for every case.

## Reporting summary

Further information on research design is available in the Nature Portfolio Reporting Summary linked to this article.

## Data availability

The data supporting the findings of this study are included in the main text and Supplementary Information. Data generated for the results presented in Figs. 1–6 are available in the Supplementary Information as Source Data files. All datasets are also accessible from the corresponding authors upon request. Source Data accompany this paper. Source data are provided with this paper.

## Code availability

Custom-developed firmware for BLE SoCs, as well as Android applications (including user interfaces) for smartphones, are available from the corresponding author upon request. The corresponding author will review all requests for source code to ensure they comply with any applicable intellectual property or confidentiality restrictions.

## References

- Franklin, D. et al. Synchronized wearables for the detection of hemodynamic states via electrocardiography and multispectral photoplethysmography. *Nat. Biomed. Eng.* **7**, 1229–1241 (2023).
- Yoo, J.-Y. et al. Wireless broadband acoustic-mechanical sensing system for continuous physiological monitoring. *Nat. Med.* **29**, 3137–3148 (2023).
- Kwon, K. et al. A battery-less wireless implant for the continuous monitoring of vascular pressure, flow rate and temperature. *Nat. Biomed. Eng.* **7**, 1215–1228 (2023).
- Heng, W. et al. A smart mask for exhaled breath condensate harvesting and analysis. *Science* **385**, 954–961 (2024).
- Kwon, K. et al. An on-skin platform for wireless monitoring of flow rate, cumulative loss and temperature of sweat in real time. *Nat. Electron.* **4**, 302–312 (2021).

6. Song, J. W. et al. Bioresorbable, wireless, and battery-free system for electrotherapy and impedance sensing at wound sites. *Sci. Adv.* **9**, eade4687 (2023).
7. Kim, J. et al. Skin-interfaced wireless biosensors for perinatal and paediatric health. *Nat. Rev. Bioeng.* **1**, 631–647 (2023).
8. Kim, J. et al. Miniaturized battery-free wireless systems for wearable pulse oximetry. *Adv. Funct. Mater.* **27**, 1604373 (2017).
9. Chen, W., Wang, Z., Wang, L. & Chen, X. Smart chemical engineering-based lightweight and miniaturized attachable systems for advanced drug delivery and diagnostics. *Adv. Mater.* **34**, 2106701 (2022).
10. Xu, S. et al. Stretchable batteries with self-similar serpentine interconnects and integrated wireless recharging systems. *Nat. Commun.* **4**, 1543 (2013).
11. Chung, H. U. et al. Skin-interfaced biosensors for advanced wireless physiological monitoring in neonatal and pediatric intensive-care units. *Nat. Med.* **26**, 418–429 (2020).
12. Wu, B. et al. Functional materials for powering and implementing next-generation miniature sensors. *Mater. Today* **69**, 333–354 (2023).
13. Min, J. et al. An autonomous wearable biosensor powered by a perovskite solar cell. *Nat. Electron.* **6**, 630–641 (2023).
14. Ding, S. et al. A fingertip-wearable microgrid system for autonomous energy management and metabolic monitoring. *Nat. Electron* <https://doi.org/10.1038/s41928-024-01236-7> (2024).
15. Ray, T. R. et al. Bio-integrated wearable systems: A comprehensive review. *Chem. Rev.* **119**, 5461–5533 (2019).
16. Park, C. et al. Supramolecular-assembled nanoporous film with switchable metal salts for a triboelectric nanogenerator. *Adv. Funct. Mater.* **27**, 1701367 (2017).
17. Petritz, A. et al. Imperceptible energy harvesting device and biomedical sensor based on ultraflexible ferroelectric transducers and organic diodes. *Nat. Commun.* **12**, 2399 (2021).
18. Fan, W. et al. High-performance stretchable thermoelectric generator for self-powered wearable electronics. *Adv. Sci.* **10**, 2206397 (2023).
19. Saifi, S. et al. An ultraflexible energy harvesting-storage system for wearable applications. *Nat. Commun.* **15**, 6546 (2024).
20. Lu, Y. et al. Decoding lip language using triboelectric sensors with deep learning. *Nat. Commun.* **13**, 1401 (2022).
21. Liu, X. et al. Microbial biofilms for electricity generation from water evaporation and power to wearables. *Nat. Commun.* **13**, 4369 (2022).
22. Wang, D. et al. Multi-heterojunctioned plastics with high thermoelectric figure of merit. *Nature* **632**, 528–535 (2024).
23. Zhang, B. et al. Nature-inspired interfacial engineering for energy harvesting. *Nat. Rev. Electr. Eng.* **1**, 218–233 (2024).
24. Gao, Z. et al. Advanced Energy Harvesters and Energy Storage for Powering Wearable and Implantable Medical Devices. *Adv. Mater.* 2404492 <https://doi.org/10.1002/adma.202404492> (2024).
25. Jixiang, G. et al. Hybrid solar evaporation system for water and electricity co-generation: Comprehensive utilization of solar and water energy. *Nano Energy* **107**, 108155 (2023).
26. Lai, Z., Xu, J., Bowen, C. R. & Zhou, S. Self-powered and self-sensing devices based on human motion. *Joule* **6**, 1501–1565 (2022).
27. Dcosta, J. V., Ochoa, D. & Sanaur, S. Recent progress in flexible and wearable all organic photoplethysmography sensors for SpO<sub>2</sub> monitoring. *Adv. Sci.* **10**, 2302752 (2023).
28. Han, D. et al. Pulse oximetry using organic optoelectronics under ambient light. *Adv. Matter Technol.* **5**, 1901122 (2020).
29. Yang, F. et al. A biomimetic-inspired approach of synthesizing colloidal persistent phosphors as a multicolor, intravital light source. *Sci. Adv.* **8**, eabo6743 (2022).
30. Martin, N. A. & Folder, S. A review of the evidence for threshold of burn injury. *Burns* **43**, 1624–1639 (2017).
31. Gastel, M. V., Stuijk, S. & Haan, G. D. New principle for measuring arterial blood oxygenation, enabling motion-robust remote monitoring. *Sci. Rep.* **6**, 38609 (2016).
32. Rwei, A. Y. et al. A wireless, skin-interfaced biosensor for cerebral hemodynamic monitoring in pediatric care. *PNAS* **117**, 31674–31684 (2020).
33. Keller, M. D., Harrison-Smith, B., Patil, C. & Arefin, M. S. Skin colour affects the accuracy of medical oxygen sensors. *Nature* **610**, 449 (2022).
34. Al-Halawani, R., Charlton, P. H., Qassem, M. & Kyriacou, R. A. A review of the effect of skin pigmentation on pulse oximeter accuracy. *Physiol. Meas.* **44**, 05TR01 (2023).
35. Chamayou-Robert, C., Digiorgio, C., Brack, O. & Doucet, O. Blue light induces DNA damage in normal human skin keratinocytes. *Photodermatol. Photoimmunol. Photomed.* **38**, 69–75 (2022).
36. Campiche, R. et al. Pigmentation effects of blue light irradiation on skin and how to protect against them. *Int. J. Cosmet. Sci.* **42**, 399–406 (2020).
37. Coats, J. G., Maktabi, B., Abou-Dahech, M. S. & Baki, G. Blue light protection, part I—Effects of blue light on the skin. *J. Cosmet. Dermatol.* **20**, 714–717 (2021).
38. Kwon, K. et al. Miniaturized, light-adaptive, wireless dosimeters autonomously monitor exposure to electromagnetic radiation. *Sci. Adv.* **5**, eaay2462 (2019).
39. Ma, Y. et al. Soft elastomers with ionic liquid-filled cavities as strain isolating substrates for wearable electronics. *Small* **13**, 1602954 (2017).
40. Yang, D. S. et al. 3D-printed epidermal sweat microfluidic systems with integrated microcuvettes for precise spectroscopic and fluorometric biochemical assays. *Mater. Horiz.* **10**, 4992–5003 (2023).
41. Choi, J. et al. Soft, skin-integrated multifunctional microfluidic systems for accurate colorimetric analysis of sweat biomarkers and temperature. *ACS Sens.* **4**, 379–388 (2019).
42. Kim, S. et al. Soft, skin-interfaced microfluidic systems with integrated immunoassays, fluorometric sensors, and impedance measurement capabilities. *PNAS* **117**, 27906–27915 (2020).
43. Oh, S. et al. Simple, miniaturized biosensors for wireless mapping of thermoregulatory responses. *Biosens. Bioelectron.* **237**, 115545 (2023).
44. Lee, C. H. et al. Soft core/shell packages for stretchable electronics. *Adv. Funct. Mater.* **25**, 3698–3704 (2015).
45. Kaneko, A., Asai, N. & Kanda, T. The influence of age on pressure perception of static and moving two-point discrimination in normal subjects. *J. Hand Ther.* **18**, 421–425 (2005).
46. Lee, K. et al. Mechano-acoustic sensing of physiological processes and body motions via a soft wireless device placed at the suprasternal notch. *Nat. Biomed. Eng.* **4**, 148–158 (2020).
47. Yoon, J. et al. GaAs photovoltaics and optoelectronics using releasable multilayer epitaxial assemblies. *Nature* **465**, 329–333 (2010).
48. Lee, J. et al. Stretchable GaAs photovoltaics with designs that enable high areal coverage. *Adv. Mater.* **23**, 986–991 (2011).
49. Park, J., Seok, H. S., Kim, S.-S. & Shin, H. Photoplethysmogram analysis and applications: An integrative review. *Front. Physiol.* **12**, 808451 (2022).
50. G. W. J. Clarke, A. D. C. Chan, A. Alder, Effects of motion artifact on the blood oxygen saturation estimate in pulse oximetry, *IEEE MeMeA*, 11-12 10.1109/MeMeA.2014.6860071 (2014).
51. Kienle, A. & Patterson, M. S. Improved solutions of the steady-state and the time-resolved diffusion equations for reflectance from a semi-infinite turbid medium. *J. Opt. Soc. Am. A* **14**, 246–254 (1997).
52. Reuss, J. L. Multilayer modeling of reflectance pulse oximetry. *IEEE trans. biomed. eng.* **52**, 153–159 (2005).
53. Walker, H. K., Hall, W. D. & Hurst, J. W. Clinical methods: the history, physical, and laboratory examinations (Butterworth press, 1990).
54. Reinhart, K. et al. Comparison of central-venous to mixed-venous oxygen saturation during changes in oxygen supply/demand. *Chest* **95**, 1216–1221 (1989).

55. Matcher, S. J. et al. Optical tomography, photon migration, and spectroscopy of tissue and model media: Theory, human studies, and instrumentation. P 486–495 (Proceedings of the SPIE press, 1995).
56. Kalra, A., Lowe, A. & Al-Jumaily, A. M. Mechanical behaviour of skin: a review. *J. Mater. Sci. Eng.* **5**, 1000254 (2016).
57. Joodaki, H. & Panzer, M. B. Skin mechanical properties and modeling: A review. *Proc. Inst. Mech. Eng., Part H: J. Eng. Med.* **232**, 323–343 (2018).
58. Kannan, S. & Ramamoorthy, M. Mechanical characterization and experimental modal analysis of 3D Printed ABS, PC and PC-ABS materials. *Mater. Res. Express* **7**, 015341 (2020).
59. Rogers, J. <https://BioRender.com/udodejl> (2025).

## Acknowledgements

This work was supported by the Querrey-Simpson Institute for Bioelectronics at Northwestern University. K.K. acknowledges support from the National Research Foundation of Korea (NRF) grant (No. RS-2022-NRO72054 and RS-2020-NRO49568) and the Institute of Information & Communications Technology Planning & Evaluation (IITP) under the Graduate School of Artificial Intelligence Semiconductor (IITP-2025-RS-2023-00256472) grant, funded by the Korea government (MSIT; Ministry of Science and ICT), and the BK21 FOUR program (Connected AI Education & Research Program for Industry and Society Innovation, KAIST EE, No. 4120200113769). Figure 1a and Supplementary Fig. 33b created with BioRender.Com released under a Creative Commons Attribution-NonCommercial-NoDerivs 4.0 International license (<https://creativecommons.org/licenses/by-nc-nd/4.0/deed.en>). Data analysis was conducted using Origin Pro 2023b, MATLAB R2023a, and FLIR ResearchIR.

## Author contributions

C.P., K.K., and J.A.R. developed the research idea, designed the overall experiments, analyzed the data, and wrote the manuscript. D.Y.P. and Y.S. designed the firmware and app for adaptive devices. D.Y. and M.Z. designed the microfluidic system and performed the colorimetric analysis. H.Z., R.A., Z.-B.H., and Y.H. conducted PPG and sweat sensor simulations. C.R.R. and A.F.S. performed the animal model test of the PPG sensor. S.Y., J.-Y.Y., T.P., A.V.-G., S.Y.H., J.K., H.-Y. A., S.O., Y.K., J.-H.K., A.B. performed the experimental validations.

## Competing interests

The authors declare no competing interests.

## Additional information

**Supplementary information** The online version contains supplementary material available at <https://doi.org/10.1038/s41467-025-60911-1>.

**Correspondence** and requests for materials should be addressed to Yonggang Huang, Kyeongha Kwon or John A. Rogers.

**Peer review information** *Nature Communications* thanks Zhiyong Fan, Xiaomin Xu, and the other, anonymous, reviewer(s) for their contribution to the peer review of this work. A peer review file is available.

**Reprints and permissions information** is available at <http://www.nature.com/reprints>

**Publisher's note** Springer Nature remains neutral with regard to jurisdictional claims in published maps and institutional affiliations.

**Open Access** This article is licensed under a Creative Commons Attribution-NonCommercial-NoDerivatives 4.0 International License, which permits any non-commercial use, sharing, distribution and reproduction in any medium or format, as long as you give appropriate credit to the original author(s) and the source, provide a link to the Creative Commons licence, and indicate if you modified the licensed material. You do not have permission under this licence to share adapted material derived from this article or parts of it. The images or other third party material in this article are included in the article's Creative Commons licence, unless indicated otherwise in a credit line to the material. If material is not included in the article's Creative Commons licence and your intended use is not permitted by statutory regulation or exceeds the permitted use, you will need to obtain permission directly from the copyright holder. To view a copy of this licence, visit <http://creativecommons.org/licenses/by-nc-nd/4.0/>.

© The Author(s) 2025

<sup>1</sup>Querrey Simpson Institute for Bioelectronics, Northwestern University, Evanston, IL, USA. <sup>2</sup>Center for Bio-Integrated Electronics, Northwestern University, Evanston, IL, USA. <sup>3</sup>Graduate School of Artificial Intelligence Semiconductor, Korea Advanced Institute of Science and Technology, Daejeon, Republic of Korea. <sup>4</sup>Department of Civil and Environmental Engineering, Northwestern University, Evanston, IL, USA. <sup>5</sup>School of Mechanical Engineering, Chung-Ang University, Seoul, Republic of Korea. <sup>6</sup>The Chicago Institute for Fetal Health, Ann and Robert H. Lurie Children's Hospital of Chicago, Chicago, IL, USA. <sup>7</sup>College of Biomedical Science & Health, Inje University, Gimhae, Republic of Korea. <sup>8</sup>Department of Biomedical Engineering, Northwestern University, Evanston, IL 60208, USA. <sup>9</sup>Department of Semiconductor Convergence Engineering, Sungkyunkwan University, Suwon, Republic of Korea. <sup>10</sup>School of Electrical Engineering, Korea Advanced Institute of Science and Technology, Daejeon, Republic of Korea. <sup>11</sup>Department of Electrical and Computer Engineering, North Carolina State University, Raleigh, NC, USA. <sup>12</sup>Center for Advanced Self-Powered Systems of Integrated Sensors and Technologies (ASSIST), North Carolina State University, Raleigh, NC, USA. <sup>13</sup>Department of Mechanical Engineering, Rice University, Houston, TX, USA. <sup>14</sup>Xingjian College, Tsinghua University, Beijing, China. <sup>15</sup>School of Chemical Engineering, Sungkyunkwan University (SKKU), Suwon, Republic of Korea. <sup>16</sup>Division of Electrical Engineering, Hanyang University ERICA, Ansan, Republic of Korea. <sup>17</sup>Weinberg College of Arts and Sciences, Northwestern University, Evanston, IL, USA. <sup>18</sup>Department of Surgery, Northwestern University Feinberg School of Medicine, Chicago, IL, USA. <sup>19</sup>Department of Materials Science and Engineering, Northwestern University, Evanston, IL, USA. <sup>20</sup>Department of Mechanical Engineering, Northwestern University, Evanston, IL, USA. <sup>21</sup>Department of Neurological Surgery, Northwestern University Feinberg School of Medicine, Chicago, IL, USA. <sup>22</sup>These authors contributed equally: Chanho Park, Do Yun Park, Haohui Zhang, Da Som Yang. ✉ e-mail: [y-huang@northwestern.edu](mailto:y-huang@northwestern.edu); [kyeongha@kaist.ac.kr](mailto:kyeongha@kaist.ac.kr); [jrogers@northwestern.edu](mailto:jrogers@northwestern.edu)